

PARAMETER EXTRACTION FOR BIPOLAR TRANSISTORS

BY

JU SUNG PARK

A DISSERTATION PRESENTED TO THE GRADUATE SCHOOL
OF THE UNIVERSITY OF FLORIDA IN PARTIAL FULFILLMENT
OF THE REQUIREMENTS FOR THE DEGREE OF
DOCTOR OF PHILOSOPHY

UNIVERSITY OF FLORIDA

1989

TO MY PARENTS

ACKNOWLEDGMENTS

I wish to express my sincere appreciation to the chairman of my supervisory committee, Professor Arnost Neugroschel, for his guidance, encouragement, and support throughout the course of this work. I also thank Professors Fredrik A. Lindholm, Gys Bosman, Sheng S. Li, and Timothy J. Anderson for their participation on my supervisory committee.

I am grateful to Dr. Konstantinos Misiakos for suggesting the topic and helping with the measurement of Auger coefficients.

I want to express my appreciation to Dr. Peter Zdebel and Mr. Victor de la Torre from Motorola Inc., for supplying devices and for their cooperation regarding the collector resistance measurement.

I want to express my appreciation to Dr. Jong-Sik Park and Dr. Tae-Won Jung, Tae-Hwan Yoon, Hanggeun Jung, and Moon-Seok Choi for many helpful discussions and encouragement.

I am indebted to my wife, Kyung Hwa, for her support and patience during all the years of this study.

The financial support of the Semiconductor Research Corporation and Electronics Telecommunication Research Institute are gratefully acknowledged.

TABLE OF CONTENTS

	Page
ACKNOWLEDGEMENT	iii
ABSTRACT	vi
CHAPTER	
ONE INTRODUCTION	1
TWO MEASUREMENT OF THE BASE RESISTANCE	6
2.1 Introduction	6
2.2 Review of Conventional Methods	8
2.3 Theoretical Background	10
2.4 Experimental Results	12
2.4.1 Base and Emitter Resistances	12
2.4.2 Extrinsic Base Resistance r_{bx}	21
2.4.3 Base-Emitter and Base-Collector Space-Charge Capacitances	23
2.4.4 Measurement of Junction Temperature and Saturation Currents	27
2.4.5 Resistance Measurement for Heterojunction Bipolar Transistors	30
2.5 Discussion	34
2.5.1 Accuracy Consideration for the Measurement of Base Resistance	34
2.5.2 Comments on the Open-Collector Method for Measurement of the Emitter Resistance r_e	35
2.6 Conclusions	37
THREE MODELING OF THE EFFECTIVE EMITTER RESISTANCE	38
3.1 Introduction	38
3.2 Basic Physics for the Contact Resistance	39
3.2.1 Classification of Contacts	39
3.2.2 Specific Contact Resistance	41
3.2.3 Contact Crowding and Transmission Line Model	41
3.3 Model for the Emitter Resistance	46
3.4 Computer Simulation	47
3.5 Results and Discussion	50
3.5.1 Computer Simulation Results	50
3.5.2 Experimental Results	61
3.6 Conclusions	63

FOUR	MEASUREMENT OF THE COLLECTOR RESISTANCE	64
4.1	Introduction	64
4.2	Review of the Conventional Methods	67
4.3	Physical Model	69
4.3.1	Upward Operation of the p-n-p Transistor	69
4.3.2	Downward Operation of the p-n-p Transistor ...	73
4.4	Experimental Results	76
4.4.1	Measurement of the Collector Resistance	76
4.4.2	Measurement of the Emitter Resistance	90
4.5	Conclusions	93
FIVE	MEASUREMENT OF THE AUGER COEFFICIENTS	97
5.1	Introduction	97
5.2	Experimental Results and Numerical Interpretation ..	99
5.2.1	Approximate Analytical Model	101
5.2.2	Numerical Analysis	107
5.2.3	Extraction of J_{on} and J_{op}	110
5.2.4	Extraction of C_A	113
5.3	Discussion	115
5.3.1	Sensitivity of C_A to other Parameters	115
5.3.2	Band Gap Narrowing and Transition Probabilities	120
5.4	Conclusions	125
SIX	SUMMARY AND SUGGESTIONS	127
APPENDICES		
A	INPUT IMPEDANCE FOR COMMON-EMITTER CONFIGURATION	130
B	INPUT IMPEDANCE FOR COMMON-BASE CONFIGURATION	132
C	FREE CARRIER ABSORPTION	134
REFERENCES	137
BIOGRAPHICAL SKETCH	143

Abstract of Dissertation Presented to the Graduate School
of the University of Florida in Partial Fulfillment of the
Requirements for the Degree of Doctor of Philosophy

PARAMETER EXTRACTION FOR BIPOLAR TRANSISTORS

By

JU SUNG PARK

August 1989

Chairman: Arnost Neugroschel
Major Department: Electrical Engineering

This dissertation deals with reliable and accurate extraction of parameters applicable to bipolar device and circuit design. The extraction is based on new methods developed as a part of this study.

Series resistances of the emitter, base, and collector are very important in determining the static and dynamic performance of bipolar transistors. An accurate small-signal impedance method for measurement of the base and emitter resistances and the junction capacitances is described. The method also yields the current dependence of the base resistance. The method is demonstrated on advanced small-size transistors with polysilicon contacts. The accuracy of the results is checked through an internal self-consistency test based on a unique subtraction method for measuring the junction capacitances.

A new method for measurement of the collector resistance was developed. The method uses the parasitic p-n-p transistor associated

with the n-p-n integrated circuit transistor. The measured collector resistance shows a sharp transition from the large low-current value to the low high-current value. The transition is due to the high injection phenomena. The measured results agree very well with numerical simulations. The method also yields the emitter resistance by combination with other DC measurement.

The Auger coefficient in the electron-hole plasma in the density range from 10^{17} to $5 \times 10^{17} \text{ cm}^{-3}$ is measured from the dependence of the electroluminescence of the $p^+-p^- - n^+$ structure on current. The new method developed for this purpose also uniquely determines the plasma density as a function of current. The range of plasma densities studied corresponds to the electron and hole concentrations in the collector of the bipolar transistor at high currents. The new measured value for the Auger coefficient is $1.77 \times 10^{-30} \text{ cm}^6 \text{ s}^{-1}$, which is about five times larger than the currently accepted value.

CHAPTER ONE INTRODUCTION

As the complexity of integrated circuits approaches the level of VLSI (Very Large Scale Integration), it is very important to predict the performance of individual semiconductor devices and circuits. This will reduce the manufacturing cost because correcting errors in VLSI circuits design requires a lot of turn-around time. To predict the performance of VLSI, we need good device and circuit simulators. The accuracy of simulators depends on accurate inputs, which include the circuit, physical device structure, and parameters of semiconductor devices. Thus, extraction of the parameters of a semiconductor device plays an important role in reducing the development cost of VLSI circuits.

There are two kinds of parameters that describe the performance of a semiconductor device: the device parameters (e.g. series resistances, capacitances, inductances) for the circuit analysis and the material parameters (e.g. mobility, bandgap, lifetime, etc.) for the device analysis. In principle, we need only the material parameters and the information about the structure (geometry and doping profiles) in order to predict the performance of the device. However, there are still large uncertainties about the values for the material parameters and the device structure. Even if these problems were solved, the simulators, which receive the material parameters as the inputs, cannot give us an accurate description of

a device due to incomplete understanding of some physical phenomena, and also due to the multidimensional effects in advanced submicrometer devices.

Considerable effort is being made to characterize the physical phenomena, measure the material parameters, and improve the device simulators, in order to extract the device parameters directly from the device simulation results. However, there still are discrepancies between simulations and experimental results because of the reasons mentioned above. Another approach is to extract the device parameters from the fabricated devices, which will serve as the input parameters for the circuit simulator, such as SPICE. The second approach is more direct and accurate than the previous approach, which starts from the material parameters and device structure as the input parameters for the device and circuit simulators.

The direct measurement of the device parameters offers a number of advantages. It provides information about devices for circuit designers who are not familiar with the details of device physics. It may also help device physicists to improve the present understanding of the device operation or, perhaps, to find unknown phenomena which are not included in the present models used by the device simulators. The results of direct measurement can also be used as criteria to determine the yield and uniformity of a certain device process.

There are many techniques for parameter extraction for bipolar transistor. The problems involved in the existing techniques are

mainly poor accuracy, inapplicability for all bias levels and devices, poor physical meaning, and complexity of the measurement. In this thesis, we suggest new techniques for measuring the device and material parameters of bipolar transistors. Seven important device parameters of a bipolar transistor (base resistance, emitter resistance, collector resistance, collector-base junction capacitance, base-emitter junction capacitance, device temperature, and junction saturation currents) will be discussed and new measurement techniques for the above parameters will be suggested and demonstrated on state-of-the-art devices. There are other parameters, not discussed in this thesis, that are required to fully describe a transistor model, such as the hybrid- π model. The parameters discussed here, however, are generally the most difficult to measure and are the key parameters that determine the transistor characteristics [1].

High speed bipolar transistors operate, for a minimum gate delay, at current density near or even exceeding the onset of the so-called high-current phenomena [2]. The high-current effects in these devices occur predominantly in the lightly doped epitaxial collector region. If the transistor operates in the high-current regime, an electron-hole plasma can be generated in the lightly doped collector region [3]. The material parameters in the electron-hole plasma may deviate from their typical low-current values due to carrier-carrier scattering and other effects [4-5]. Bandgap narrowing, ambipolar mobility, and Auger recombination coefficients in the plasma state are important for characterization of the high-

current regime of the bipolar transistor. In this thesis, Auger recombination will be discussed and a new measurement technique for this parameter will be introduced.

In Chapter Two, several published measurement techniques for the base resistance will be briefly reviewed. Then, our new technique for measurement of the base resistance and the junction capacitances will be introduced. Emphasis is placed on reliable measurements of small-size transistors with examples shown for Si bipolar transistors with emitters smaller than $10 \mu\text{m}^2$. Advantages over measurements on large-area test devices are discussed. The method serves as the basis for the measurement of other parameters, such as the current-dependence of base resistance, emitter resistance, space-charge region capacitances of the base-emitter and base-collector junctions, junction temperature, and base and collector saturation currents. Applications to heterojunction bipolar transistors are also demonstrated.

In Chapter Three, we will exploit the contact crowding [6-7] and emitter crowding [8], to develop a new model for an effective current-dependent emitter resistance. The emitter resistance is considered in all present models as current independent. However, we will show that the effective emitter resistance may vary with current and depends on many variables. The effective emitter resistance is investigated in our model as a function of bias, geometry, sheet resistances of the base and emitter, and emitter specific contact resistance. The model is experimentally verified by measurements on two extreme device cases.

In Chapter Four, a new measurement technique for collector resistance will be introduced. The new technique uses the parasitic p-n-p transistor of the main n-p-n transistor. By operating the parasitic p-n-p transistor in the upward and downward modes, we can separate various components of collector resistance. Through the accurate value of collector resistance, we can also obtain the emitter resistance. Our new technique is demonstrated on various transistors and compared with numerical simulations.

In Chapter Five, we present a new technique for measuring Auger coefficients in the electron-hole plasma. Auger coefficients are determined by comparing the measured electroluminescence with the numerically calculated plasma density of a $p^+-p^-n^+$ diode. The effects of series resistance are removed by plotting electroluminescence versus current. Another advantage of the electroluminescence method is that it uniquely determines the plasma density as a function of current.

CHAPTER TWO MEASUREMENT OF THE BASE RESISTANCE

2.1 Introduction

The base resistance r_b depends on the geometry and the base sheet resistance R_{SB} , which is inversely proportional to the integrated neutral base impurity density. In high-performance transistors, the base width is very narrow ($\approx 1000 \text{ \AA}$). For a typical base-emitter junction doping gradient of 10^{24} cm^{-4} , the space-charge region width shrinks from about 300 \AA at zero bias to about 150 \AA at 0.75 V [9]. The narrowing of the space-charge region width widens the quasi-neutral base and, thus, reduces r_b [10]. Other effects that lower r_b at high current are conductivity modulation and base push-out [11-13]. Numerical calculation of the current dependence of r_b is possible [14-16] but requires a detailed knowledge of the base doping profile, doping dependence of the majority-carrier mobility in the base, and in small devices, also a consideration of two- or three-dimensional effects. The emitter resistance consists of the resistance of the emitter bulk and the contact resistance. The contact resistance is usually dominant for heavily doped emitter. The emitter bulk resistance can be calculated numerically. The contact resistance is technology dependent and has to be determined by measurement. Thus, a direct measurement of the base and emitter

resistances is important not only for circuit design, but also for verification of the accuracy of the process and device models.

In this chapter, we present and demonstrate new methods for accurate and reliable measurement of the base (r_b) and the emitter (r_e) series resistances and their current dependencies. We also determine the base-emitter and base-collector space-charge region capacitances, temperature of the device under test, and the base and collector saturation currents. A self-consistency check (via measured capacitances) to assure the accuracy and reliability of the measurements on small-size transistors is described. The new method eliminates the need for a dummy device normally required in standard direct capacitance measurements. An analysis of the I_C - V_{BE} curve to give accurate junction temperature and saturation current is proposed. The analysis is based on a correction of the measured I_C - V_{BE} curve for the effects of basewidth modulation by V_{BE} .

In Section 2.2, we briefly review conventional methods for measuring r_b and point out their deficiencies. In Section 2.3, we present the theoretical background for the new measurement. The experimental results for Si transistors with various sizes and application for GaAlAs/GaAs heterojunction transistor are also shown in Section 2.4. Accuracy considerations for measurement of series resistances are discussed in Section 2.5.

2.2 Review of Conventional Methods

Traditionally, r_b has been a difficult parameter to measure. The main reason is that r_b is modeled as a lumped resistance, although it is actually a distributed resistance. Modeling of r_b by a single lumped resistance simplifies circuit analysis of complex circuits. As a result of the use of the lumped r_b , the value obtained for r_b depends strongly on the measurement technique used and on the transistor operating conditions. Some of the conventional techniques are reviewed below.

In the DC technique the voltage deviation of the base current from an exponential ideal dependence is measured. The voltage divided by the base current gives r_b [17]. This technique is not valid for the scaled-down advanced bipolar transistors with polysilicon contacts because the voltage deviation includes the $I_E r_e$ contribution in addition to the $I_B r_b$ term. The $I_E r_e$ drop may be negligible for transistors with large emitter metal-contact area, but is not negligible for advanced bipolar transistors where r_e can be large because of small emitter size. Even for large emitters with metal-contacts, there is a problem with this technique because r_e increases due to the current crowding. In Chapter Three the increase in r_e will be discussed.

Since the noise performance is one of the device characteristics that is significantly influenced by the value of r_b , it is natural to attempt to measure noise to determine r_b [18-19]. This type of measurement is not popular because of problems with shielding and noise measurement.

The semi-circle method uses the input impedance of the common-emitter configuration [20-21]. The impedance of the base-emitter junction modeled by the hybrid- π transistor model is plotted on the complex impedance plane with frequency as a variable. The locus forms a semi-circle. The right intercept of the semi-circle on the real axis occurs at zero frequency. The impedance value at this point is the sum of r_{π} , r_b , and $(1+\beta)r_e$. The extrapolated value of the left intercept, which occurs at the infinite frequency, is the sum of r_b and r_e . The diameter of the circle depends on current. It is very large at small currents and very small at large currents. The locus, calculated from a simple one-lump model, is not an exact semi-circle [22]; thus, a semi-circle fit to the measured data yields errors for intercepts. At high frequencies, the parasitic and stray capacitances cause additional distortions. For these reasons, the accuracy of this method is questionable, particularly at small currents. Another disadvantage of this technique is the time required to obtain the data for various biases and the difficulty in predetermining the collector current at which r_b can be accurately measured.

The phase cancellation method [23] uses the input impedance of the common-base configuration. The collector current is varied until a certain value (I_{cm}) at which the input capacitance is zero. At this condition, the resistance reading is the sum of r_b , r_e , and $kT/(qI_{cm})$. This method is not applicable for transistors with large base resistances and low value of β , and for devices operating at high current, since this technique assumes $r_b \ll r_{\pi}$. There are other

techniques described in [24], but these techniques are not commonly used due to their complexity and poor accuracy. One approach, which is not a direct measurement method, is numerical simulation [14-16, 25]. As mentioned in Chapter One, this approach requires accurate knowledge of material parameters and other information for good accuracy. Thus this approach cannot yield an accurate absolute value for r_b , but it can predict the general dependence of the base resistance as a function of current or voltage.

2.3 Theoretical Background

Neugroschel [26] demonstrated a small-signal impedance method to measure low-current values of r_b and emitter resistance r_e . The method was demonstrated on relatively large transistors with the base-emitter area $A_{BE} \approx 150 \mu\text{m}^2$. In this chapter, we present a modified method [27], which removes the uncertainties of the original technique and extends the application of the method [26] to small-size device, down to $A_{BE} \approx 1 \mu\text{m}^2$. Measurement of r_b on actual small-size devices is essential to reveal multi-dimensional effects. The standard approach of using large-area devices to measure r_b and then do scale-down this value to small-size device is not accurate, since the scaling does not necessarily applies to r_b .

The method presented [26] is based on measurement of two input impedances of a transistor at small $V_{BE} \leq 0.4 \text{ V}$; the common emitter (CE) impedance Z_{ine} and the common base (CB) impedance Z_{inb} .

To derive the input impedances Z_{ine} and Z_{inb} , we start from the hybrid- π representation of a bipolar transistor. We assume, as

Neugroschel did [26], that the effective base-emitter dynamic resistance $r_{\pi} \gg 1/\omega C_{\pi}$. This condition can be easily satisfied for any transistor for $V_{BE} \leq 0.4$ V at frequency $f \approx 50$ MHz. Other assumptions used in the derivation are given and justified in Appendix A. The expression for $Z_{ine} = R_{ine} - jX_{ine}$ is derived in Appendix A (see (A.2)) and is given here for convenience

$$R_{ine} = r_{bx} + r_{bi} \left(\frac{C_{\pi} + C_{\mu}}{C_{ine}} \right)^2 + r_e \left(\frac{C_{\pi}}{C_{ine}} \right)^2 \quad (2.1)$$

$$1/X_{ine} = \omega C_{ine} = \omega (C_{\pi} + C_{\mu} + C_{sc}) = \omega (C_{\pi} + C_{jc}), \quad (2.2)$$

where C_{ine} is the total measured capacitance and equal to the sum of all capacitances of the equivalent circuit, and C_{jc} is the total base-collector space-charge region capacitance.

For the CB configuration we make use of Fig. B.1 (given in Appendix B) and obtain the following expression for Z_{inb} (see (B.2))

$$R_{inb} = r_{bx} + r_{bi} + r_e \quad (2.3)$$

$$1/X_{inb} = \omega C_{inb} = \omega C_{\pi}. \quad (2.4)$$

For a typical transistor with $R_{SB} = 10$ k Ω /square, $r_b = r_{bx} + r_{bi} \gg r_e$ for small bias levels and

$$R_{inb} \approx r_b. \quad (2.5)$$

There are two main differences between the CE and CB expressions. First, R_{inb} does not include capacitances, which is an

advantage in a comparison with R_{ine} . Second, C_{inb} gives directly the equivalent base-emitter capacitance C_{π} , while C_{ine} includes all capacitances of the equivalent circuit.

2.4 Experimental Results

2.4.1 Base and Emitter Resistances

The transistors used to demonstrate the new methods in this work were fabricated using a single layer poly-silicon process with a poly-silicon emitter contact and a metal base contact. The emitter size in these devices is very close to the mask size, except for a very small lateral emitter diffusion. The transistors have non-walled emitters with mask sizes of $2 \times 4 \mu\text{m}^2$, $2 \times 12 \mu\text{m}^2$, and $2 \times 100 \mu\text{m}^2$, and a single-stripe base contact. The devices measured were mounted in T0-5 headers.

In Fig. 2.1, the solid line shows the measured dependence of $R_{inb} \approx r_b$ on V_{BE} for the transistor with $2 \times 12 \mu\text{m}^2$ emitter. The data were obtained at a frequency $f = 38 \text{ MHz}$ with $V_{BC} = 0 \text{ V}$ using a Hewlett-Packard HP4194A impedance analyzer. The measurement instrument was zeroed with a dummy device before the readings of Z_{inb} were taken. The measured resistances and capacitances were nearly frequency independent in the range from 20 to 40 MHz as shown in Fig. 2.2. Further comments on importance of zeroing of parasitics using a dummy device will be presented in Section 2.5.1.

The measured R_{inb} decreases nearly linearly with increasing V_{BE} , in an agreement with numerical predictions [14-16]. The sharp increase in R_{inb} for $V_{BE} > 0.4 \text{ V}$ is due to the violation of the

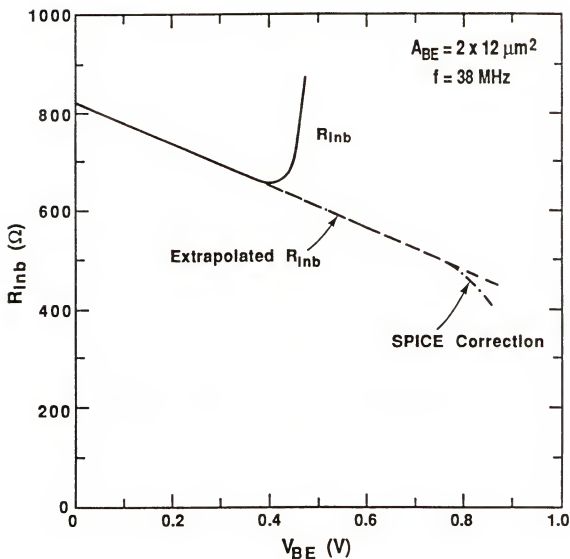


Fig. 2.1 Measured common-base input resistance R_{inb} as a function of base-emitter voltage V_{BE} . The dashed line is the linearly extrapolated dependence.

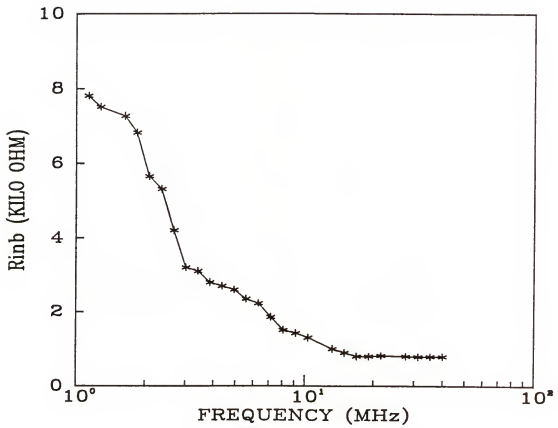


Fig. 2.2 Measured common-base input resistance R_{inb} for emitter area of $2 \times 12 \mu\text{m}^2$ as a function of frequencies ($V_{BE} = 0.3 \text{ V}$).

assumption $r_{\pi} \gg 1/\omega C_{\pi}$ (see Appendix B). Beyond this voltage, (2.3) and (2.4) are not valid. To find R_{inb} for higher voltages, we linearly extrapolate the measured R_{inb} dependence, as shown in Fig. 2.1 by the dashed line. It was verified experimentally [28], by measuring the pinch resistance of a transistor base with two base contacts, that the extrapolation is valid as long as the lateral voltage drop $r_b I_b \ll kT/q$ ($\approx 26\text{mV}$ at 300 K). The validity of the extrapolation was also verified numerically [14-16]. For $r_b I_b \geq kT/2q$, the current crowding becomes significant, which causes a sharp decrease in r_b [29]. The transistor of Fig. 2.1, $r_b I_b < 5\text{ mV}$ for $V_{BE} < 0.9\text{ V}$.

Figure 2.3 shows the measured I-V curves for the $2 \times 12\text{ }\mu\text{m}^2$ transistor. The base current I_B deviates for $V_{BE} > 0.8\text{ V}$ from its nearly ideal $\exp(qV_{BE}/kT)$ dependence by

$$\Delta V = r_b I_B + r_e I_E. \quad (2.6)$$

Equation (2.6) is valid for any V_{BE} , provided that I_B is due to the recombination in the heavily doped emitter, which remains in low injection. The effect of r_e on ΔV is not negligible, even if $r_e \ll r_{bi}$, since $I_E = (1+\beta)r_e I_B$.

To find r_e , we combine ΔV from Fig. 2.3 with $r_b \approx R_{inb}$ from Fig. 2.1. For the V_{BE} range from 0.8 V to 0.85 V, we find that ΔV varies from 7 to 25 mV. Using (2.6) we find that $r_e = 10\text{ }\Omega$. A more accurate SPICE analysis (see Chapter Three), using a filament transistor model with 20 sections, yields only a small correction

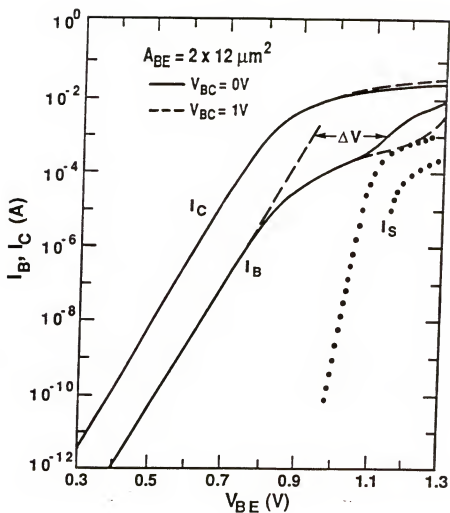
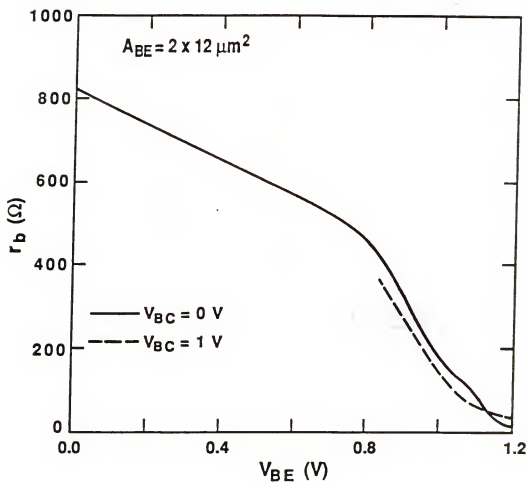


Fig. 2.3 Measured dependencies of the base and collector currents on V_{BE} for two values of V_{BC} . The dashed line extending the I_B plot is the ideal base current proportional to $\exp(qV/kT)$. The dotted curves are for the substrate current I_S for $V_{CS} = 0\text{V}$ (upper curve) and 0.2V (lower curve).

shown in Fig. 2.1 by the dashed-dotted line and gives $r_e = 10.2 \, \Omega$. Similar analysis for a $2 \times 100 \, \mu\text{m}^2$ transistor gave $r_e = 2.2 \, \Omega$. Assuming that r_e is due mainly to the contact, this corresponds to the specific emitter contact resistance of $\rho_c = r_e A_{BE} = 236 \, \Omega \cdot \mu\text{m}^2$ and $\rho_c = 360 \, \Omega \cdot \mu\text{m}^2$, respectively.

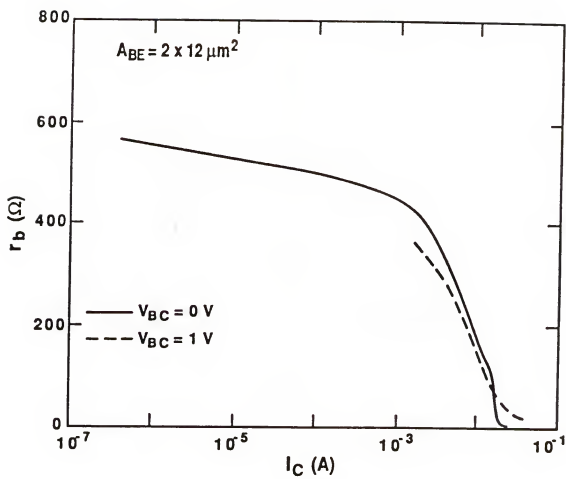
In spite of the fact that current crowding occurs for $V_{BE} > 0.85 \, \text{V}$, the emitter current through the emitter contact will still be essentially uniform (see Chapter Three), and r_e will remain at the low-current value determined above (assuming that ρ_c is constant). This allows calculating r_b with (2.6) as a function of V_{BE} or the collector current I_C . The results are shown in Fig. 2.4 (a) and (b).

The kink in the I_B versus V_{BE} curve in Fig. 2.3 at $V_{BE} \approx 1.1 \, \text{V}$ is due to the forward-biasing of the base-collector junction by the voltage drop $I_C R_C$ on the collector resistance R_C , which contributes to I_B in addition to the contribution from the base-emitter junction (see Chapter Four). Corresponding kinks seen in the r_b versus V_{BE} and r_b versus I_C plots in Fig. 2.4 (a) and (b) are due to the modulation of r_b by injection from the forward biased base-collector junction. The $I_C R_C$ drop will also forward bias the collector-substrate junction causing I_S to flow into the substrate. The kink in I_B - V_{BE} plot can be also caused by the emitter current of a parasitic p-n-p transistor flowing into the base. The substrate current, I_S , measured for $V_{BC} = 0 \, \text{V}$ and two values of the collector-substrate reverse bias, $V_{CS} = 0$ and $0.2 \, \text{V}$, is shown in Fig. 2.3 by the dotted lines. It is clear from Fig. 2.3 that $I_S \ll I_B$ (note



(a)

Fig. 2.4 The total base resistance r_b as a function of (a) V_{BE} and (b) I_C .



(b)

Fig. 2.4 (continued)

also that I_B is the same for both values of V_{CS}). This clearly shows that the kink in the I_B - V_{BE} curve is not caused by I_S for the transistor of Fig. 2.3. The fact that I_S flows into the substrate and not out of the substrate was verified by observing the polarity of I_S . The deviation of I_C from the ideal exponential dependence is determined not only by ohmic losses (ΔV), but also by other high-current effects. As a result, no visible kink in $\ln(I_C)$ versus V_{BE} is observed, although a small kink is observed when the plot of I_C versus V_{BE} is displayed on a linear scale.

The broken lines in Fig. 2.4 (a) and (b) show the r_b plots for $V_{BC} = 1$ V. Compared to the zero bias case, the reverse bias narrows the base thickness, which increases the low-current r_b , but decreases the current-crowding onset voltage. The low-current portion of the r_b dependence for $V_{BC} = 1$ V could not be measured with the present experimental setup. At high currents, r_b will probably saturate at a value close to r_{bx} . For $V_{BE} > 1.1$ V, however, our procedure for measuring r_b is not very reliable. One reason is a possible heating of the junction due to large I_C . In addition (2.6) uses the assumption that I_B is due to the recombination in the emitter only. This assumption may be violated because of the large density of holes and electrons recombining within the base and collector. The recombination at high currents has to account for the bandgap narrowing induced by the electron-hole plasma [30], which further increases the current.

Results for R_{inb} for the three transistors measured are shown in Table 2.1. Since the emitters in these transistors are non-walled, the calculation of the base sheet resistance from R_{inb} is not straightforward and depends on the layout as well as other variables [25,31].

2.4.2. Extrinsic Base Resistance r_{bx}

Because r_{bx} can be considered as current independent, except for very high currents, it can be conveniently determined from the zero-bias values of $R_{ine}(0)$ and $R_{inb}(0)$. If $C_\mu \ll C_\pi$, which is a good approximation because the base-emitter space-charge region capacitance per unit area is about 10 times larger than that of the base-collector junction (see Tables 2.2 and 2.3); then,

$$r_{bx} \approx R_{inb}(0) - r_{bi}(0)$$

$$= \frac{R_{ine}(0) - R_{inb}(0) [(C_\pi + C_\mu)/C_{ine}]^2}{1 - [(C_\pi + C_\mu)/C_{ine}]^2}. \quad (2.7)$$

Because of coupling between the active and inactive base, a separation of the total base resistance r_b into r_{bi} and r_{bx} is possible only for transistors with walled emitters or for transistors with very long emitter stripe. Since transistors with walled emitters were not available, the measurement was done for a $2 \times 100 \mu m^2$ transistor and yielded $r_{bx} \approx 6 \Omega$.

Table 2.1 Summary of the measured results for the base resistance.

Emitter Mask Size (μm^2)	C_S (fF)	R_S (Ω)	C_{inb} (fF)	ΔC_{par} (fF)	$R_{inb(0)}$ (Ω)
2 x 4	30.4	1023	21	+9.4	2143
2 x 12	70.8	904	73.5	-2.7	839
2 x 100	568	129.9	589	-21	121

Table 2.2 Summary of the measured base-collector space-charge region capacitances. The zero-bias capacitance $C_{jc(0)}$ is obtained from (2.8).

Emitter Mask Size (μm)	C_{CE} (fF)	C_{CB} (fF)	$C_{jc(0)}$ (fF)	A_{BC} (μm^2)
2 x 4	117	95	23	8 x 10
2 x 12	201.5	143.5	58	16 x 10
2 x 100	1048	694	354	104 x 10

Table 2.3 Summary of the measured base-emitter space-charge region capacitances. C_{CE} and C_{CB} are the measured capacitances for the inverted emitter-down transistors.

Emitter Mask Size (μm^2)	C_{CE} (fF)	C_{CB} (fF)	$C_{je(0)}$ (fF)
2 x 4	117	96	21
2 x 12	201.5	128	73.5
2 x 100	1059	470	589

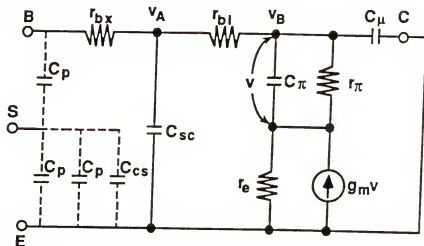
2.4.3. Base-Emitter and Base-Collector Space-Charge Capacitance

To determine the base-collector space-charge region (junction) capacitances C_{jc} , we measure the input CE and CB capacitances. The measured input capacitances will, in addition to the intrinsic capacitances C_{ine} and C_{inb} given by (2.2) and (2.4), include the parasitic capacitance. The parasitic capacitance C_p , due to the bondpads and metallization over the oxide, will appear in the equivalent diagrams in Fig. 2.5 between the terminals and the substrate which is left floating. It can be shown that, for conditions in which (2.3) and (2.4) are valid, the parasitic capacitances C_{cs} , including the collector-substrate capacitance, can be coupled into one effective capacitance C_{par} between the input base and emitter terminals for both the CE and CB configurations as shown in Fig. 2.5 (a) and (b). The total input capacitances are then $C_{CE} = C_{ine} + C_{par}$ and $C_{CB} = C_{inb} + C_{par}$. Thus, using (2.2) and (2.4) we obtain

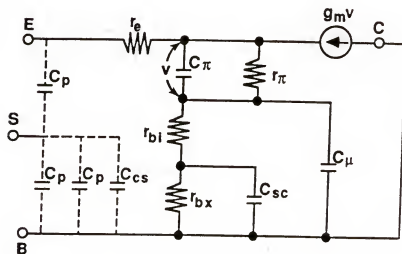
$$C_{CE} - C_{CB} = (C_{ine} + C_{par}) - (C_{inb} + C_{par}) = C_{jc}. \quad (2.8)$$

The base-collector capacitance is obtained simply by subtracting the two measured input capacitances. Similarly, the base-emitter junction capacitance C_{je} is obtained from measurements of the inverted emitter-down transistor.

One important difference between the new method and the standard direct measurement of junction capacitances is that accurate direct measurement requires perfect zeroing by a dummy



(a)



(b)

Fig. 2.5 The equivalent circuits of common-emitter (a) and common-base (b) for a transistor. C_p and C_{cs} at the inputs are the stray capacitances between the bonding pads and the substrate and the collector-substrate capacitance, respectively.

device. This is not possible for small devices in which the parasitic capacitances are much larger than the intrinsic capacitances because of variations over the wafer in oxide thickness and geometry, and also because the metal coverage for the dummy is different from that for the active transistor in the vicinity of the contact holes. Additional error may be due to the stray capacitances of the probe tips for on-wafer probing. Because our method does not require the dummy device, the measurement error due to zeroing is practically eliminated. The measurement can be done without disconnecting the probes by using a jumper to short the collector to the emitter or to the base. Both input capacitances can be measured with an accuracy of about ± 0.3 fF allowing measurement on devices with $A_{BE} = 1 \mu\text{m}^2$. The measuring frequency can be as low as 1 MHz, or less, making on-wafer measurements relatively easy.

The results for the zero-bias capacitances $C_{jc}(0)$ and $C_{je}(0)$ in three different transistors measured at a frequency of 1 MHz are summarized in Tables 2.2 and 2.3. The results of on-wafer measurements for MOSAIC III devices are shown in Table 2.4. Column 3 in Table 2.4 shows the results of the direct measurement method, $C_{je}(\text{Mot})$, for comparison. The agreement is excellent except for the smallest devices. This shows, that both techniques are accurate. The subtraction method using (2.8) will be, however, more reliable for smaller devices because of the reasons discussed briefly above. The method can be used for any reverse bias. The applicability for

Table 2.4 Summary of on-wafer measurements for MOSAIC III devices.

Emitter Mask Size (μm^2)	C_{jc} (fF)	$C_{jc}(\text{Mot})$ (fF)	C_{je} (fF)	$C_{je}(\text{Mot})$ (fF)
1.5 x 4	15.8	17.0	21.1	19.0
1.5 x 4	16.2	17.0	20.6	20.0
2 x (1.5 x 4)	30.7	32.0	39.4	39.0
1.5 x 8	25.4	26.0	38.1	38.0
1.5 x 12	34.0	34.0	57.2	56.0
2 x (5.75 x 16.5)	188.8	186.0	392.6	393.0
2 x (5.75 x 16.5)	189.3	186.0	396.7	391.0
6 x (2 x 19)	321.7	322.0	633.7	613.5
2 x 12	36.5	37.0	67.2	66.0
2 x 8	27.9	27.0	44.7	45.0
2 x (2 x 4)	33.1	34.0	47.9	47.5
2 x 4	18.1	18.0	25.5	24.0
2 x 4	17.5	17.0	25.9	24.0

forward bias is limited by the requirement $\omega C_{\pi} \gg r_{\pi}$, and breaks down for $V_{BE} \geq 0.4$ V (see Fig. 2.1).

C_{je} can be accurately extrapolated to higher voltages either numerically [32] or analytically [9] from the measured $C_{je}(0)$. The calculations for $V_{BE} > 0.8$ V should include the effects of the electron-hole plasma in the SCR [30]. This effect is generally ignored, but recent calculations show that the electron-hole plasma will increase the capacitance by as much as a factor of three to four in a comparison with standard values [33].

2.4.4. Measurement of Junction Temperature and Saturation Currents

The ideal collector current of a bipolar transistor and the base sheet resistance $R_{SB} \propto r_{bi}$ can be expressed by standard relations:

$$I_C = \frac{A q n_i^2 \exp(qV_{BE}/kT)}{\int_0^{W_b} \frac{N_B(x)}{D_n(x)} dx}$$

$$= \frac{A q n_i^2 \bar{D}_n \exp(qV_{BE}/kT)}{\int_0^{W_b} N_B(x) dx} = I_{C0} \exp(qV_{BE}/kT) \quad (2.9)$$

$$R_{SB} = \left(\int_0^{W_b} q \mu_p(x) N_B(x) dx \right)^{-1}$$

$$\approx \left(q \bar{\mu}_p \int_0^{W_b} N_B(x) dx \right)^{-1}, \quad (2.10)$$

where $N_B(x)$ is the position dependent base doping, \bar{D}_n is the spatially averaged minority-carrier diffusion coefficient in the base, and $\bar{\mu}_p$ is the spatially averaged majority-carrier mobility in the base. The junction temperature can be obtained using (2.9) from $kT/q = dV_{BE}/d(\ln I_C)$. This is strictly valid only if the width of the quasi-neutral base W_b remains constant with increasing V_{BE} . But, as Fig. 2.1 clearly indicates, W_b increases (measured R_{inb} decreases) with increasing V_{BE} . Since I_C depends inversely on the integrated neutral base impurity density, the measured I_C varies with V_{BE} as $I_{C0} \exp(qV_{BE}/mkT)$ with the voltage dependent slope factor $m(V_{BE}) > 1$. Thus,

$$dV_{BE}/d(\ln I_C) = m(V_{BE})kT/q. \quad (2.11)$$

Equation (2.11) cannot be used to obtain the accurate junction temperature, because the voltage dependent slope factor $m(V_{BE})$ is not known. To obtain the correct temperature from I_C , we have to make a correction to account for the W_b variation with V_{BE} . This can be done approximately by taking the ratio of (2.9) and (2.10)

$$I_C/R_{SB} = Aq^2 n_i^2 (\bar{D}_n \bar{\mu}_p) \exp(qV_{BE}/kT). \quad (2.12)$$

The parameters \bar{D}_n and $\bar{\mu}_p$ are somewhat voltage dependent, but it can be shown numerically that in the V_{BE} range from, e.g., 0.4 V to 0.8 V, the dominant factor causing the R_{inb} decay shown in Fig. 2.1 is the integrated base doping. Taking $\bar{D}_n \bar{\mu}_p$ as V_{BE} independent

gives $I_C/R_{SB} = C \exp(qV_{BE}/kT)$, where C is a temperature-independent constant, and

$$dV_{BE}/d(\ln(I_C/R_{SB})) = kT/q. \quad (2.13)$$

The slope given by (2.13) is independent of V_{BE} and yields the correct junction temperature T . A correction for the voltage dependence of $\bar{D}_n \bar{\mu}_p$ can be made numerically, if the base doping is known.

To illustrate the procedure we give here the results of analysis for a $2 \times 100 \mu m^2$ transistor. The saturation current I_{C0} obtained from the measured I_C - V_{BE} curve depends on the range of voltage chosen. The least square fit for the range from 0.34 V to 0.7 V yields $kT/q = 25.84$ mV ($T = 299.6$ K) and $I_{C0} = 2.6 \times 10^{-16}$ A. Using the range from 0.5 V to 0.7 V gives kT/q mV ($T = 300.76$ K) and $I_{C0} = 2.83 \times 10^{-16}$ A. The I_C/r_{bi} dependence gives a straight line with the slope $kT/q = 25.51$ mV ($T = 295.94$ K) and $I_{C0} = 2.2 \times 10^{-16}$ A using $r_{bi}(0) = r_b(0) - r_{bx} = 121 \Omega - 7 \Omega = 114 \Omega$. Using the correct T we find the slope factor $m \approx 1.012 - 1.016$ for the measured I_C . The ambient temperature monitored by a precision thermistor with an accuracy of ± 0.2 K was $T = 296.26$ K.

The discrepancy of about 4 K between the actual T and that obtained from the I_C dependence corresponds to the ratio of the intrinsic carrier concentrations of about $n_i^2(300 \text{ K})/n_i^2(296 \text{ K}) = 2$. This discrepancy is important if we want to verify the accuracy of device simulators or analytical models by comparing the measured I_C

and I_B with calculations (which require the temperature as an input). The discrepancies between I_{C0} from the I_C - V_{BE} and (I_C/r_{bi}) - V_{BE} curves will be much larger at smaller temperatures. For example, at $T = 100$ K, an extrapolation of I_C from $V_{BE} = 1$ V to $V_{BE} = 0$ V with the slope factor of $m = 1.015$ will overestimate I_{C0} by a factor of about 5.

Saturation currents depend on material parameters, such as mobility, bandgap narrowing, doping profile, etc., and are, therefore, the main measured parameters from which the above transport parameters are extracted. This cannot be done without accurate and reliable determination of the saturation currents and the corresponding device temperature.

The measured $\ln I_B$ - V_{BE} curves for the devices tested also shows $m > 1$. Thus, a direct extrapolation gives an error in I_{B0} . The error is minimized by taking $I_{B0} = I_{C0}/\beta_{max}$, where I_{C0} is found from (2.16) and β_{max} is the maximum DC current gain. It is reasonable to assume that, for V_{BE} at which $\beta = \beta_{max}$, the space-charge region recombination is minimized.

2.4.5 Resistance Measurements for Heterojunction Bipolar Transistors

Resistance analysis of HBTs using the DC I - V curves is particularly difficult because typical I - V curves are very non-ideal. This makes even an estimate of resistance using DC methods difficult. To illustrate this, we show in Fig. 2.6 a typical I_B - V_{BE} curve for an n-p-n GaAlAs/GaAs HBT that follows an $I_B \approx \exp(qV/mkT)$ dependence with $m = 1.5$ to 1.9. This indicates that I_B is dominated

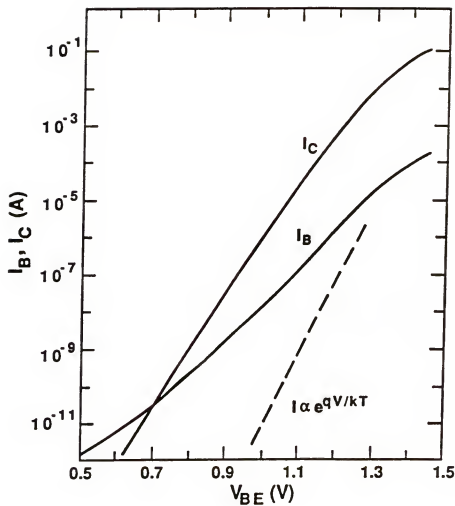


Fig. 2.6 I_C - V_{BE} and I_B - V_{BE} characteristics for a heterojunction GaAlAs/GaAs transistor. The dashed line is a reference line with an ideal exponential voltage dependence.

by the SCR recombination current. The I_C - V_{BE} curve gives $m \approx 1.05$. The transistor was fabricated by LPE growth method and has a circular geometry with a diameter of $60 \mu\text{m}$. The base width is about $0.2 \mu\text{m}$ and is uniformly doped with about 5×10^{18} acceptors/ cm^3 . Analysis of series resistances for transistor with such non-ideal base current using DC techniques is not possible, since they require an ideal $\exp(qV/kT)$ component as a reference current. Our AC technique does not have this restriction and is ideally suited for the analysis of HBTs. The results are shown in Fig. 2.7 (a) and (b). Figure 2.7 (a) shows the measured resistances R_{inb} and R_{ine} as a function of V_{BE} . Figure 2.7 (b) displays the resistances r_{bi} and r_{bx} obtained from (2.1), (2.3), and (2.7). In contrast to the Si case of Fig. 2.1, the r_{bi} for the HBT is almost current independent because the base is heavily and uniformly doped, which makes the R_{SB} modulation due to V_{BE} negligible. Because of large bandgaps of GaAlAs and GaAs, the applicability of the ac method extends about $V_{BE} \approx 1 \text{ V}$. The large base doping makes the intrinsic and extrinsic base resistances comparable, and they can be both determined accurately. The extrinsic resistance r_{bx} includes the base contact resistance, which appears to be very important in limiting the speed of HBT [34-35]. The emitter resistance was negligible for the very large test transistor and could not be found accurately. However, for small-size HBTs, which were not available for testing, all three resistances can be measured.

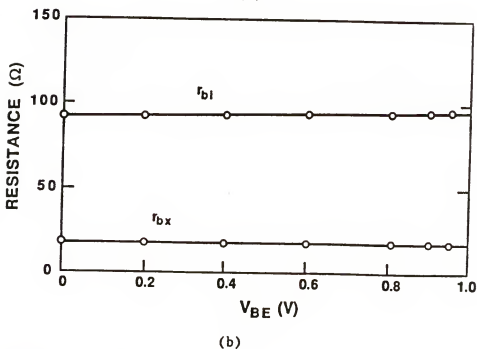
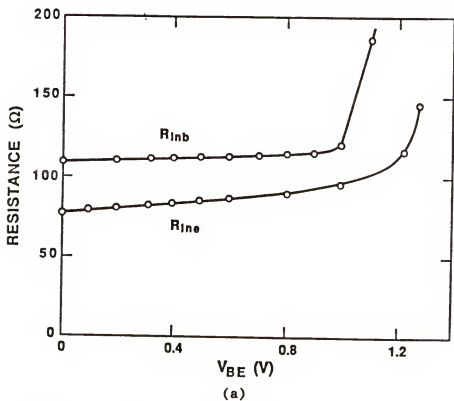


Fig. 2.7 Measured results for the heterojunction transistor.

- (a) Measured input resistances for the common-base and common-emitter for the HBT from Fig. 2.6.
 (b) The base intrinsic and extrinsic resistances versus V_{BE} from (a).

2.5 Discussion

2.5.1 Accuracy Considerations for Measurement of Base Resistance

The procedure for measuring the base resistance using the common-base configuration requires compensation of parasitics by zeroing with a dummy device. For a perfect zeroing, the measured values R_S and C_S , are equal to the intrinsic parameters R_{inb} and C_{inb} given by (2.3) and (2.4). Since our method uses frequency $f \leq 50$ MHz, the transmission line effects of the parasitics can be neglected and they can be considered to be nearly pure capacitors. Since a perfect zeroing for C_{par} is not possible, an error ΔC_{par} gives $C_S = C_{inb} \pm \Delta C_{par}$, and

$$R_S = R_{inb} \left(\frac{C_{inb}}{C_{inb} \pm \Delta C_{par}} \right)^2 = R_{inb} \left(\frac{C_{inb}}{C_S} \right)^2. \quad (2.14)$$

To be sure that no error in R_{inb} is caused by assuming that $\Delta C_{par} = 0$, we need a self-consistency test for the zeroing procedure that would give us the residual uncompensated or overcompensated ΔC_{par} (either positive or negative) and C_{inb} . This is particularly important for small devices where $C_{par} \gg C_{inb}$. The correct R_{inb} can be then obtained from (2.14), in spite of imperfect zeroing. The compensation offset ΔC_{par} is obtained from two measured values as $\Delta C_{par} = C_S - C_{inb}$. As pointed out above, C_{inb} for the inverted emitter-down transistor is found very accurately from $C_{inb} = C_{CE} - C_{CB}$. This measurement is immune to parasitics because of the subtraction involved.

Table 2.1 shows the measured values R_S , C_S , and $C_{inb} = C_{je}$ (see Table 2.3). Notice that ΔC_{par} is positive for the $2 \times 4 \mu m^2$ device, but is negative for the other two devices. The last column in Table 2.1 shows the corrected values for $r_b \approx R_{inb}$ obtained using (2.14).

We have found that most reliable and reproducible results are obtained by measuring both the dummy device and the active device in a parallel equivalent mode. The capacitance and conductance of the dummy device are then subtracted from those for the active device and converted to the series values R_S and C_S .

2.5.2 Comments on the Open-Collector Method for Measurement of the Emitter Resistances r_e

The open-collector method is the most commonly used techniques to measure r_e . The method requires only DC measurement of the collector-emitter saturation voltage V_{CES} as a function of I_B with the collector open-circuited. The emitter resistance is then calculated from $r_e \approx dV_{CES}/dI_B$ [24]. Some modifications of this procedure are suggested in [36-37]. Figure 2.8 shows the V_{CES} dependence on I_B for the $2 \times 12 \mu m^2$ transistor. The reciprocal slope of the dashed line taken at $V_{CES} \approx 30$ mV gives $dV_{CES}/dI_B = 17.5 \Omega$. The dependence is not linear and suggests that r_e decreases with increasing I_B . For example, $dV_{CES}/dI_B \approx 14 \Omega$ at $V_{CES} \approx 80$ mV. It is easy to show that neither of these values is possible. To demonstrate that we go to Fig. 2.3 and translate the measured I_B - V_{BE} curve to the left by the voltage drop $(-\Delta V) = I_E r_e$ for $V_{BE} \leq 1$ V. The corrected I_B , using the open-collector values for r_e , will be on

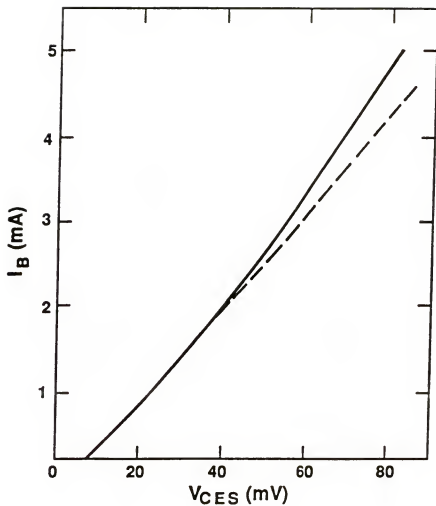


Fig. 2.8 Collector-emitter saturation voltage as a function of base current for the $2 \times 12 \mu m^2$ for measurement of emitter resistance by flyback method.

the left of the ideal dashed line (even without considering the $r_b I_b$ contribution to ΔV), which is not possible. The open-collector method clearly overestimates r_e . The correct value for $r_e = 10.2 \, \Omega$ was found previously using our method. Another technique for measuring r_e will be suggested in Chapter four.

2.6 Conclusions

New measurement methods for accurate analysis of submicrometer-emitter bipolar transistors were presented. Measurement of the base resistance for a wide range of collector current was demonstrated. The new method for the measurement of the space-charge region capacitances does not require the use of a dummy device for the compensation of the parasitics, which avoids zeroing errors occurring in standard capacitance measurements. The accuracy of about ± 0.3 fF for the measurement of the base-emitter and base-collector capacitances can be employed to study the effects of process variations in order to optimize the speed. The ability to measure small-size transistors, instead of using large test devices, can be used to investigate yield, uniformity across the wafer, and multi-dimensional effects. The measurements suggested in this paper can be performed at frequencies from about 1 to about 40 MHz. This relatively low frequency range makes on-wafer testing feasible.

CHAPTER THREE MODELING OF THE EFFECTIVE EMITTER RESISTANCE

3.1 Introduction

In the most widely used common-emitter (CE) configuration the emitter resistance is amplified by the CE current gain (β). Thus, an accurate analysis of the emitter resistance is necessary for exact transistor modeling. The emitter resistance is usually considered to be dependent only on the physical parameters of a transistor. However, as will be shown later, the emitter resistance also varies with current because of contact and emitter crowding. The emitter resistance at low current levels is simply determined by the emitter contact resistance. The emitter resistance at the operating point where the emitter crowding is significant has two components. The first component is from the interface layer of the contact, the second one is from the semiconductor layer under the contact hole.

In Section 3.2 we introduce physics necessary to characterize the contact resistance. In Section 3.3 we develop new model for the accurate evaluation of the emitter resistance as a function of current. The extraction method for the emitter resistance based on the new model is suggested in Section 3.4. Section 3.5 presents the computer simulation results and the experimental results. Conclusions will be given in Section 3.5.

3.2 Basic Physics for the Contact Resistance

3.2.1 Classification of Contacts

The contacts of semiconductor devices can be classified into two types, the horizontal-type or the vertical-type, depending on the direction of the current flow in the semiconductor under the planar contact. For a better illustration, a cross-section of a bipolar transistor is shown in Fig. 3.1. Near the base contact region, the current flows mostly horizontally, which causes current crowding at the contact edge. This characterizes the horizontal-type contact. Since most of the collector current in the integrated circuit transistor flows through the heavily-doped buried layer, the current under the collector contact flows almost vertically. Thus, the collector contact is an example of a vertical-type contact. The emitter contact belongs to both types, depending on the bias level and other factors. At the bias level where the emitter crowding is not significant, the emitter contact acts as a vertical contact. As the emitter crowding becomes significant, the emitter contact may become the horizontal-type contact, or in between the horizontal and vertical types. Most of the contacts in MOS belong to the horizontal-type. Many efforts were made to characterize the horizontal-type contact for MOS and other devices [38-45]. The characterization for the emitter contact is more complicated than for a pure horizontal-type because of the reasons mentioned above.

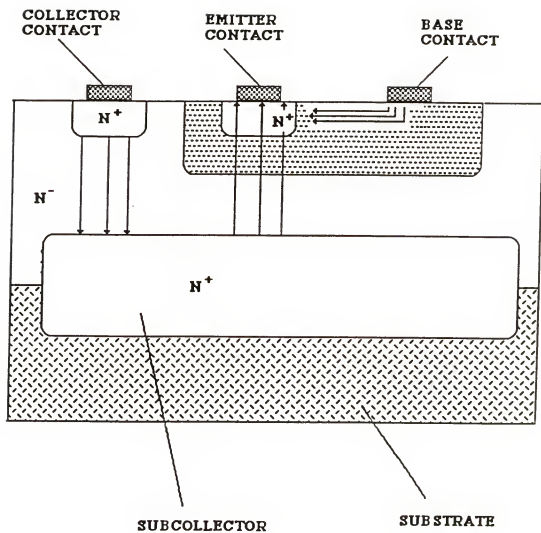


Fig. 3.1 Cross-section of a planar n-p-n transistor with the main current flows indicated by arrows.

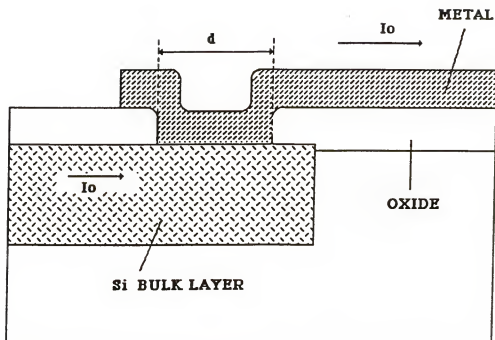
3.2.2 Specific Contact Resistance

The specific contact resistance (ρ_c) in $\Omega\text{-cm}^2$ is defined as the resistance of unit area of the interfacial layer between two conduction layers and is expressed as the ratio of voltage drop across the interfacial layer to the current density. The carrier transport through the interfacial layer is governed by the thermionic emission over the barrier and tunneling through the barrier [46]. The relative magnitude of the two components depends on the barrier height, temperature, doping concentration, and other factors. For low doped samples, the thermionic emission component dominates over the tunneling component. When the doping concentration is high, the depletion region width near the interface in the semiconductor becomes very narrow. Therefore, carriers can easily tunnel through the barrier.

3.2.3 Contact Crowding and Transmission Line Model

Using the definition of ρ_c , we can easily estimate the resistance value for the vertical contact. But, the contact resistance for the horizontal contact cannot be easily expressed by $R_c = \rho_c / \text{Area}$, because the current density through the contact hole is not uniform due to the so-called contact crowding [6-7]. Figure 3.2 shows the cross-section of a contact and its distributed equivalent circuit. In Fig. 3.2 (b),

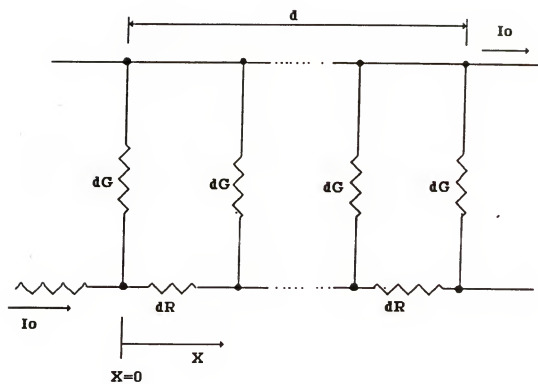
$$dR = \frac{R_s}{W} dx \quad (3.1)$$



(a)

Fig. 3.2 Schematic illustration of a contact hole for the modeling of contact crowding.

- (a) Cross-section of a contact hole. Current flows into the left edge of the contact hole and flows out from the right edge.
- (b) Transmission-Line Model for the contact depicted in (a).



(b)

Fig. 3.2 (continued)

$$dG = \frac{W}{\rho_c} dx, \quad (3.2)$$

where R_s , W , and dX are the sheet resistance of the semiconductor layer under the contact hole, the width of the contact hole, and the length of a single lump of the distributed model, respectively. The resistance component of the metal layer is neglected because of its small resistivity. The current flowing to the contact edge in the semiconductor layer will travel through the path which gives the minimum resistance.

Muramann and Widmann [6] and Berger [7] modeled the contact resistance by a Transmission Line Model (TLM), which is widely used for characterizing the horizontal-type contact [35-45]. To qualitatively understand the basic concept of the contact crowding, let us assume that $d \ll W$, where d is the length of a contact. Then the current distribution $j(x)$ across the contact hole can be expressed by

$$j(x) = \frac{I_0}{W} \sqrt{\alpha} \frac{\cosh \sqrt{\alpha}(x - d)}{\sinh \sqrt{\alpha}d}, \quad (3.3)$$

where I_0 is the total current through the contact lead, $\alpha = (R_s/\rho_c)^{1/2}$, and R_s is the sheet resistance of the semiconductor layer under the contact.

The current distribution across the contact hole for various values of $y = x(R_s/\rho_c)^{1/2}$ is shown in Fig. 3.3. The contact with the higher R_s , longer d , and smaller ρ_c has heavier contact

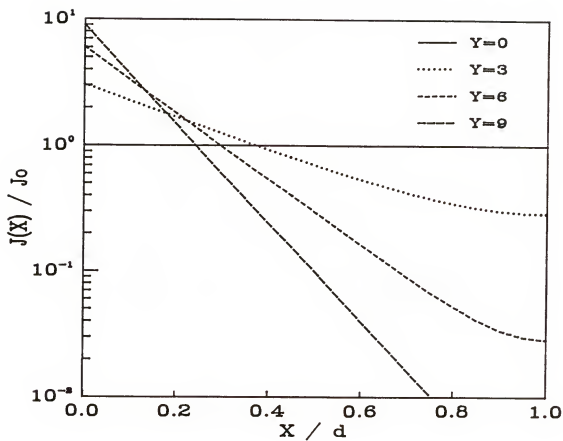


Fig. 3.3 Current distribution across the contact hole shown in Fig. 3.2.

crowding. This means that the effective resistance of this kind of contact is larger than the value from the simple formula $R_C = \rho_C / \text{Area}$. Note also that for $y = 0$ the current flows uniformly across the contact. This situation occurs for very small R_S or very large ρ_C .

3.3 Model for the Emitter Resistance

As discussed in Section 3.2, the emitter contact of a bipolar transistor can be classified into one of two categories depending on the operating condition. For the emitter contact to operate as an ideal horizontal-type contact, the emitter current should flow only into the one side of the contact. This cannot, however, occur in a real transistor as is explained below. Since the tendency of the emitter current to flow into one side of the emitter contact is controlled by the emitter crowding, we have to accurately analyze the emitter crowding. Although many authors treated the problem of the emitter crowding [8, 29], their approaches are not applicable for our case because they neglected the contribution of the emitter resistance to the emitter crowding. This neglect overestimates the emitter crowding, because the negative feedback from the emitter resistance is not taken into the account.

A single transistor can be modeled as a combination of elementary one-dimensional transistors [15]. By adding TLM for the emitter contact to this combination of elementary transistors, we obtain the equivalent circuit shown in Fig. 3.4. For a simplification of the analysis, we make the following assumptions:

- (1) the current gain β is independent of position and current,
- (2) the base conductivity modulation and push-out are negligible, and
- (3) the emitter has a butted structure.

Although the above assumptions cause some error, they are reasonable in a sense that the results give a correct trend for the emitter resistance dependence on current, ρ_c , sheet resistances of the base and emitter, and geometry. This is also confirmed experimentally. The transistor shown in Fig. 3.4 has the width of W and the length of d . The elements of Fig. 3.4 are defined as follows

$$\Delta R_B = R_{SB} \cdot \Delta d / W \quad (3.4)$$

$$\Delta R_{EV} = \frac{\rho_c}{\Delta d \cdot W} \quad (3.5)$$

$$\Delta R_{EL} = \frac{R_{SE} \cdot \Delta d}{W}, \quad (3.6)$$

where R_{SB} is the base sheet resistance, R_{SE} is the emitter sheet resistance, $\Delta d = d/N$, and N is the numbers of the elementary transistors used in modeling.

3.4 Computer Simulation

In the previous Section, we have developed an equivalent circuit model for the purpose of modeling the emitter resistance. Our next step is to extract the effective emitter resistance from the model. From Fig. 3.4, we can derive a set of nonlinear

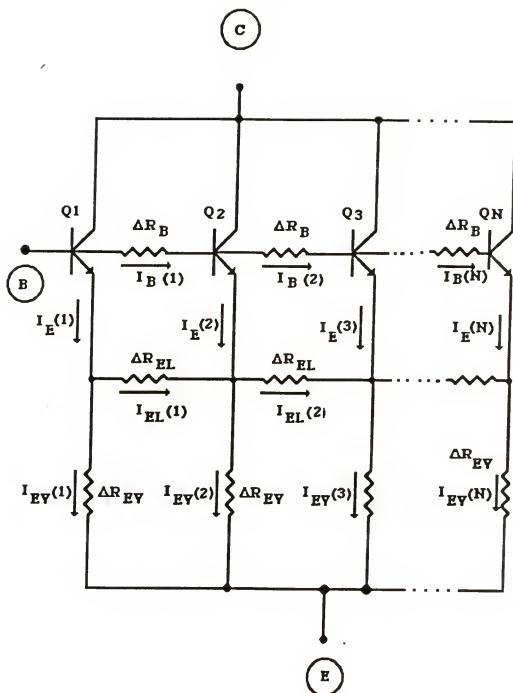


Fig. 3.4 Equivalent Circuit of sectioned transistor model.

ΔR_{EV} and ΔR_{EL} represent the resistances from interface layer of contact hole and emitter bulk(n^+).

differential equations with respect to position x , $V_{BE}(x)$, and $I_B(x)$. These equations can be solved numerically. It is easier, however, to analyze the circuit of Fig. 3.4 using the circuit simulator SLICE, which is a modified version of SPICE by HARRIS. Another advantage of using SLICE is that we can easily sweep all elements of the circuit. If a transistor is divided into enough number of elementary transistors, the results from SLICE will be equivalent to the solution of the differential equations. We confirmed the validity of using SLICE by comparing the base resistance values for the single-base contact from SLICE with the values from the well-known 1oe current formula ($R_B = R_{SB}d/3W$). If a transistor is divided into 20 elementary transistors, the deviation between the two approaches is within 5%. The simulation shown below uses 20 elementary transistors. We varied four basic parameters, and selected the values of the parameters as close as possible to the values for the real devices. The ranges for four parameters are:

$$R_{SB} = 3,000 \text{ to } 11,000 \text{ } \Omega/\text{square}$$

$$\rho_C = 10 \text{ to } 200 \text{ } \Omega\text{-}\mu\text{m}^2$$

$$R_{SE} = 3 \text{ to } 20 \text{ } \Omega/\text{square}$$

$$d = 0.5 \text{ to } 10 \text{ } \mu\text{m}.$$

The results from the SLICE simulation give only the voltages at the nodes and the currents through the elements. From these, we have to extract the resistance values for the emitter and base resistances. The power dissipation concept [31] was used in calculating R_B and R_E :

$$R_B = \frac{\sum_{i=1}^{20} I_{Bi}^2 \cdot \Delta R_B}{I_B^2} \quad (3.7)$$

$$R_E = \frac{\sum_{i=1}^{20} (\Delta R_{EV} \cdot I_{EV}(i)^2 + \Delta R_{EL} \cdot I_{EL}(i)^2)}{I_E^2}, \quad (3.8)$$

where I_B , I_E , $I_B(i)$, $I_{EV}(i)$, and $I_{EL}(i)$ are base terminal current, emitter terminal current, the base current of an elementary transistor at a certain position (i), and emitter current through the interface layer of the contact and the semiconductor layer in the emitter at a certain position (i), respectively. The vertical resistance component of the emitter region is neglected due to heavily-doped shallow emitter. The first term of (3.8) represents the emitter resistance component from the interface layer of the emitter contact. The second term of (3.8) represents the emitter resistance from the n^+ layer.

3.5 Results and Discussion

3.5.1 Computer Simulation Results

For the understanding of the emitter and contact crowding of a transistor, we first consider Fig. 3.5 that shows the current distribution for $V_{BE} = 0.85$ V, $R_{SB} = 6000$ Ω/square , $\rho_c = 30$ $\Omega\text{-}\mu\text{m}^2$, $w = 10$ μm , and $d = 5$ μm . The y-axis of this graph represents the normalized values of each current to its value at $x = 0.25$ μm . The

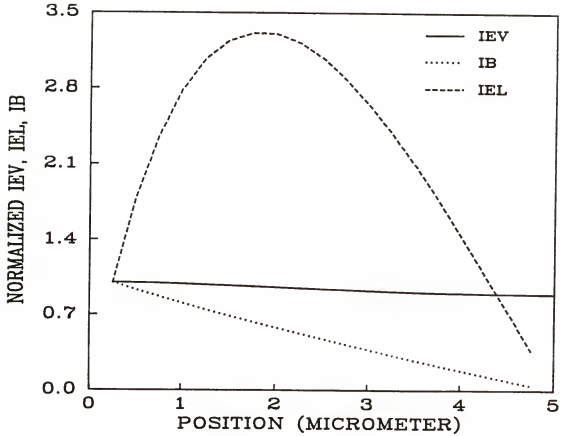


Fig. 3.5 Current distributions for the transistor in Fig. 3.4. I_{EV} , I_{EL} , and I_B are the currents through ΔR_{EV} , ΔR_{EL} , and ΔR_B , respectively. Emitter length $d = 5 \mu\text{m}$, specific contact resistance of the emitter contact $\rho_c = 30 \Omega\text{-}\mu\text{m}^2$, $V_{BE} = 0.85 \text{ V}$, the base sheet resistance $R_{SB} = 6000 \Omega/\text{square}$, and the emitter sheet resistance $R_{SE} = 10 \Omega/\text{square}$.

currents at $x = 0.25 \mu\text{m}$ correspond to the first transistor in Fig. 3.4, since a transistor with $d = 5 \mu\text{m}$ is divided into 20 elementary transistors. The single base contact is located at $x = 0 \mu\text{m}$. The base current $I_B(i)$ decreases with increasing x because the elementary transistors far away from the base contact have less forward bias at the base-emitter junction than the transistors near the base contact due to voltage drop in the base. This phenomena is well-known as the emitter crowding. As the emitter current crowds near the base contact, the emitter contact starts to act as the horizontal-type contact. The emitter currents $I_E(i)$ of the transistors in the heavy emitter-crowding zone will not pass entirely through ΔR_{EV} connected to each transistor. If the entire emitter current of each transistor flows into ΔR_{EV} connected to it, the emitter resistance becomes large due to the significant contribution from $\Delta R_{EV} = \rho_c / (\Delta d \times W)$. Thus, $I_{EV}(i)$ flows more uniformly compared to the base and emitter currents. We can easily understand this mechanism, if we check the distribution of the current I_{EL} flowing through ΔR_{EL} . The emitter current of Q_1 in Fig. 3.4 passes partially through ΔR_{EV1} , the rest flows through the next ΔR_{EL} . This tendency continues until $I_E(i)$ becomes larger than $I_{EV}(i)$. Thus, I_{EL} in Fig. 3.5 increases due to the contribution from the rest of the emitter currents of the previous transistors which have enough emitter currents in supplying $I_{EV}(i)$. After the peak point, I_{EL} decreases to support insufficient $I_E(i)$ in supplying $I_{EV}(i)$.

A) The effect of the emitter crowding:

Since the tendency for the emitter current to flow into one side of the emitter contact depends on the emitter crowding, the heavier emitter crowding causes heavier contact crowding. The emitter crowding is a function of R_{SB} , d , and V_{BE} . Fig. 3.6 displays the effective emitter resistance (R_{EFF}), normalized to low current value of ρ_c/Area , as a function of d . R_{EFF} increases with the emitter length and becomes larger for the higher R_{SB} at the same emitter length. The dependence of R_{EFF} on V_{BE} is depicted in Fig. 3.7. Figures 3.6 and 3.7 support our idea: the contact crowding becomes significant for heavy emitter crowding.

B) The effect of the contact crowding:

If the emitter crowding occurs, we have to also consider the contact crowding to properly model R_{EFF} . We cannot apply the theory developed by Murramann and Widmann [6] and Berger [7] to the emitter contact of bipolar transistor, because the emitter current does not flow into the one side of the emitter contact, but is rather distributed (see Fig. 3.5). It is hard to evaluate the emitter resistance analytically. Thus, we rely on computer simulation. To investigate R_{EFF} as a function of the contact crowding, we use the following parameters:

$$\rho_c = 10 \text{ } \Omega\text{-}\mu\text{m}^2 \text{ to } 250 \text{ } \Omega\text{-}\mu\text{m}^2 \text{ for } R_{SE} = 5, 10, 15 \text{ } \Omega/\text{square}$$

$$d = 0.5 \text{ } \mu\text{m} \text{ to } 10 \text{ } \mu\text{m} \text{ for } \rho_c = 10, 60, 110 \text{ } \Omega\text{-}\mu\text{m}^2.$$

First, we consider the effect of ρ_c and R_{SE} on the emitter resistance. In Fig. 3.8, R_{EFF}/R_{E0} decreases as ρ_c increases. For

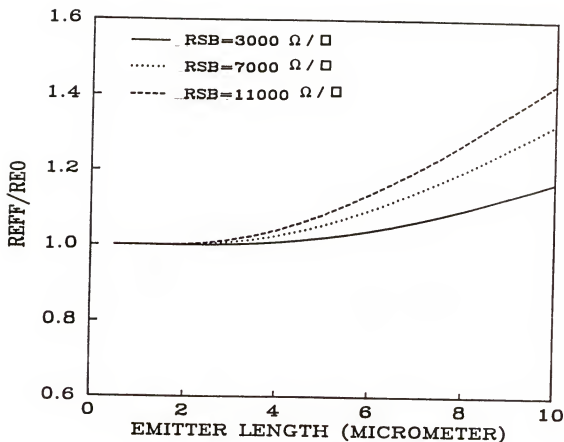


Fig. 3.6 Effective emitter resistance R_{EFF} as a function of emitter length. R_{EFF} is normalized to the low current emitter resistance (ρ_c/Area). ($V_{BE} = 0.9 \text{ V}$, $R_{SE} = 10 \Omega/\text{square}$, $\rho_c = 50 \Omega\text{-}\mu\text{m}^2$, $d = 10 \mu\text{m}$)

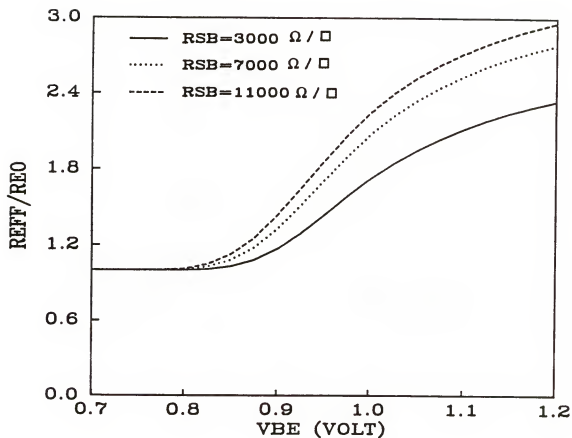


Fig. 3.7 Effective emitter resistance R_{EFF} as a function of V_{BE} .
 ($R_{SE} = 10 \Omega/\text{square}$, $\rho_c = 50 \Omega\text{-}\mu\text{m}^2$, $d = 10 \mu\text{m}$,
 $R_{SB} = 7000 \Omega/\text{square}$)

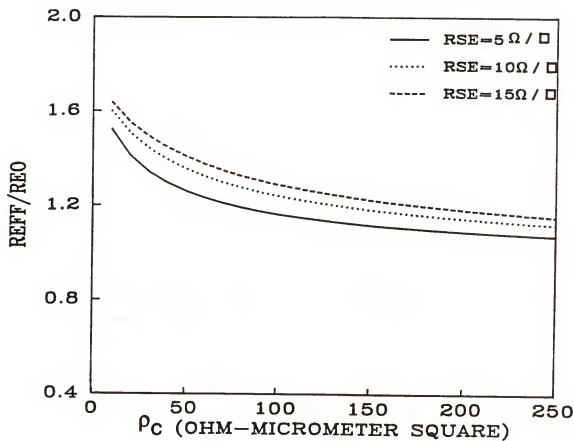


Fig. 3.8 Effective emitter resistance as a function of the specific contact resistance. ($V_{BE} = 0.9$ V, $R_{SB} = 7000 \Omega/\text{square}$, $R_{SE} = 10 \Omega/\text{square}$, $d = 10 \mu\text{m}$)

smaller ρ_c , the emitter currents of the transistors in the current crowding region have a strong tendency to flow through ΔR_{EV} instead of traveling further across the emitter region. If ρ_c is large, the emitter currents tend to spread to many parallel ΔR_{EV} branches to reduce the resistance from the interfacial layer. R_{EFF}/R_{E0} approaches unity at high ρ_c for $R_{SE} = 5 \text{ } \Omega/\text{square}$, but for $R_{SE} = 10$ and $15 \text{ } \Omega/\text{square}$ it does not approach unity because of the high lateral resistance component from the emitter region. This will be discussed in the next paragraph. Figure 3.9 shows that R_{EFF}/R_{E0} increases with increasing emitter length d . This is because for long d we have both heavy emitter and contact crowding.

C) The components of the emitter resistance:

In Fig. 3.10, we illustrate the distribution of I_{EL} for three various values of V_{BE} . Since the emitter current flows vertically at low current, there is no horizontal potential difference in the emitter region. At low V_{BE} , I_{EL} is uniform and its value is negligible compared to the total emitter current. For example, $I_{EL}(\text{peak}) = 5.16 \times 10^{-8} \text{ A}$ and $I_E = 3.07 \times 10^{-5} \text{ A}$ for $V_{BE} = 0.75 \text{ V}$. Thus, the emitter resistance at low current is due primarily to the contact resistance. But, we cannot neglect the horizontal component of the emitter resistance due to the contact and emitter crowding at high currents. For $V_{BE} = 0.85 \text{ V}$ the peak value of I_{EL} is $4.77 \times 10^{-5} \text{ A}$ and $I_E = 9.73 \times 10^{-4} \text{ A}$. Then, the contribution of ΔR_{EL} is not negligible in calculating the emitter resistance according to (3.8), because the sum of $I_{EL}(i)$ is comparable to I_E . The two components of the emitter resistance are shown in Fig. 3.11. It is clear that the

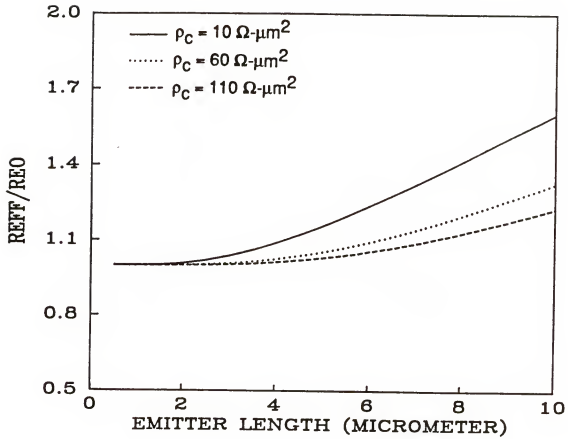


Fig. 3.9 Effective emitter resistance as a function of emitter length. ($V_{BE} = 0.9 \text{ V}$, $R_{SB} = 7000 \Omega/\text{square}$, $R_{SE} = 10 \Omega/\text{square}$, $\rho_C = 50 \Omega\text{-}\mu\text{m}^2$)

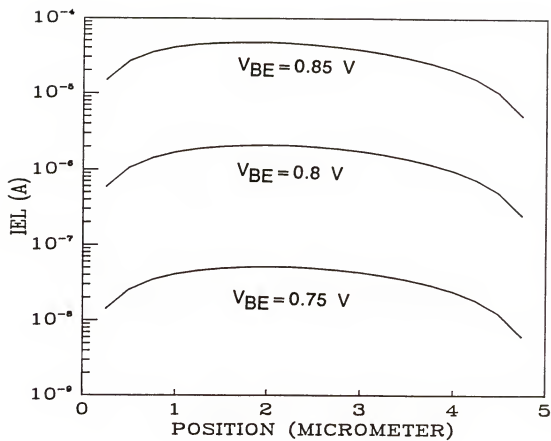


Fig. 3.10 Current distribution along ΔR_{EL} as a function of V_{BE} ,
 ($R_{SB} = 7000 \text{ } \Omega/\text{square}$, $R_{SE} = 10 \text{ } \Omega/\text{square}$, $\rho_c = 50 \text{ } \Omega\text{-}\mu\text{m}^2$,
 $d = 10 \text{ } \mu\text{m}$)

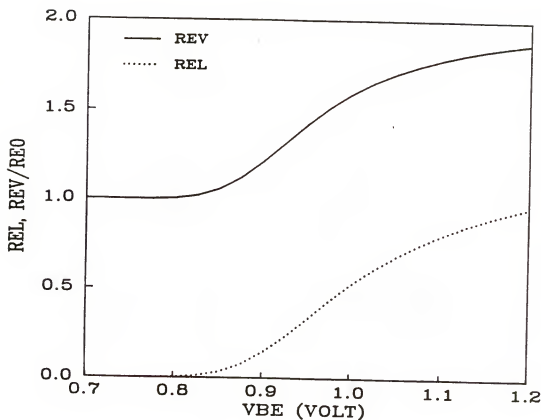


Fig. 3.11 Variation of the emitter resistance components as a function of V_{BE} . The solid line is for the contact resistance. The dotted line is for the emitter bulk resistance. ($R_{SE} = 7000 \Omega/\text{square}$, $R_{SB} = 10 \Omega/\text{square}$, $\rho_c = 50 \Omega\text{-}\mu\text{m}^2$, $d = 10 \mu\text{m}$)

lateral resistance component (ΔR_{EL}) contributes to the emitter resistance at high V_{BE} . We can also see that the vertical component (ΔR_{EV}) increases as V_{BE} increases.

3.5.2 Experimental Results

By rearranging equation (2.6), we obtain

$$\frac{\Delta V}{I_E} = \frac{R_B}{1+\beta} + R_E. \quad (3.9)$$

The first term of the right hand side of (3.9) either decreases [15] or remains constant with increasing V_{BE} if R_B/β is current independent [47]. We compared two extreme cases of the emitter contacts represented by two different devices. The devices are a metalcontact transistor with the emitter size of $25 \times 25 \mu\text{m}^2$ and a polysilicon-contact transistor with the emitter size of $2 \times 12 \mu\text{m}^2$. The reason for choosing these devices is that the metalcontact device can have a strong emitter and contact crowding due to long d and low ρ_c (ρ_c of the metalcontact device is smaller than that for the polysilicon device). On the other hand, the polysilicon-contact device has a weak emitter and contact crowding because of its short d and large ρ_c ($\rho_c = 250 \Omega\text{-}\mu\text{m}^2$ for this device [27]). Figure 3.12 shows the experimental results. For easy comparison of the two devices, the y-axis displays $\Delta V/I_E$ normalized to its peak value. $\Delta V/I_E$ for the metal-contact device continuously increases up to $V_{BE} = 1.0 \text{ V}$, but the polysilicon-contact device has the opposite dependence. The $\Delta V/I_E$ increase for the metalcontact device is caused

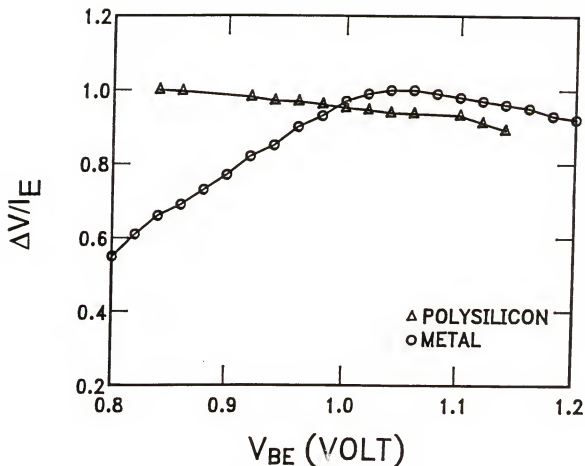


Fig. 3.12 Experimental results for two transistors with different contact materials and size. The emitter contact sizes are $2 \times 12 \mu\text{m}^2$ and $25 \times 25 \mu\text{m}^2$ for polysilicon and metal contacts, respectively. For easy comparison, the y-axis ($\Delta V/I_E = R_E + R_B/(1 + \beta)$) is normalized to the peak value for both devices.

by the increase of R_E due to the heavy emitter and contact crowding, which agrees with the simulation results in Section 3.5.1. The $\Delta V/I_E$ decrease after $V_{BE} = 1.0$ V is the result of the base conductivity modulation by high injection phenomena. Computer simulation results in Section 3.5.1 pointed out that the transistor with low R_{SB} has only small small increase in R_E . Thus, the metal-contact transistor has small R_E increase or constant R_E beyond $V_{BE} = 1.0$ V.

3.6 Conclusions

Through the computer simulation based on our new model, we have found that the emitter resistance increases as a function of current. The dependence of the emitter resistance on physical parameters was also investigated. The resistance consists of components from the contact hole and the bulk emitter region. The simulation results were checked by measuring devices with metal and polysilicon contacts. The experimental results show that the emitter resistance of the metal-contact transistor with relatively large emitter length increases at high current. This conclusion is important for the design of analog transistors and power transistors, which in most cases have long emitter with metalcontact.

CHAPTER FOUR MEASUREMENT OF THE COLLECTOR RESISTANCE

4.1 Introduction

The delay time of the Emitter Coupled Logic (ECL) consists of several time-constants, which are determined by the series resistances and capacitances of a transistor and its load resistance. The delay time can be expressed as a the sum of eight time-constants [1]. The resistance, which includes the collector series resistance (R_C) and the actual load resistance, contributes to five out of eight time-constants. Thus, R_C plays an important role in limiting the speed of digital circuits. Another important aspect of R_C in the digital applications is that, together with the emitter resistance and the internal saturation voltage $V_{CE(sat)}$, it determines the value of the logical low state. The transition frequency (f_T) of a transistor is used as a figure of merit in estimating the frequency response of a transistor in the analog application. The f_T is also a strong function of the R_C , together with other parameters of a transistor.

Therefore, R_C is a crucial parameter in estimating the switching speed and frequency response of the bipolar transistor. It is also one of the most difficult parameters to measure due to its strong dependence on bias and its distributed nature.

The collector resistance of an integrated bipolar n-p-n transistor, shown in Fig. 4.1, consists of the vertical portion R_{CV}

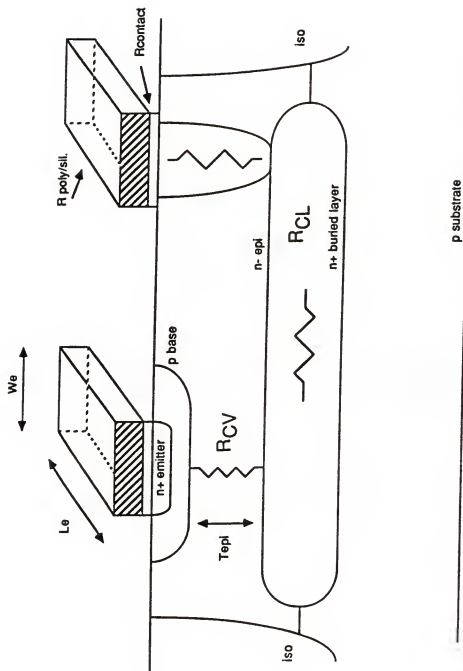


Fig. 4.1 Device cross-section showing the different components of R_C .

of the n-type epitaxial region between the edge of the base-collector space-charge region and the n^+ subcollector, the lateral portion of the n^+ subcollector, and another vertical portion of the n^+ plug between the subcollector and the collector contact. The contact resistance has to be also considered.

The heavily doped portions of R_C plus the contact resistance are current independent and will be lumped together into one resistance R_{CL} . The value of the vertical portion $R_{CV} \approx \rho_{epi} t_{epi} / A_{BE}$, is a complicated function of current, voltage, and doping. At low currents, the thickness of quasi-neutral epitaxial collector t_{epi} depends on the base-collector junction voltage, that determines the junction space-charge region width. At high currents, the base-collector junction may become forward-biased resulting in a conductivity modulation of the epitaxial region that lowers R_{CV} . The epitaxial layer will be also modulated by base-pushout at high currents. To accurately model R_C , we have to measure it as a function of current and biasing conditions. We present here two DC methods for measuring R_{CL} and R_{CV} . The methods are demonstrated on advanced MOSAIC III self-aligned polysilicon transistors.

The existing methods for measuring the R_C will be reviewed in Section 4.2. The basic concept of our new method for measuring R_C will be discussed in Section 4.3. In Section 4.4, the detailed measurement procedure will be introduced and the results for various samples are shown and discussed.

4.2 Review of the Conventional Methods

A short critical review of the published methods to measure R_C is presented here. Detailed description is presented elsewhere [24].

The high-current value $R_C(\text{sat})$ and the low-current value $R_C(\text{normal})$ of R_C can be estimated from the I_C - V_{CE} characteristics of a transistor. $R_C(\text{normal})$ can be estimated from the slope of a line drawn through the "knees" of the I_C - V_{CE} curves for different values of the base current I_B . It is very difficult, however, to determine the "knees" for each curve. Also, $R_C(\text{normal})$ from this measurement cannot represent the values for the entire forward-active region, since $R_C(\text{normal})$ depends strongly on the collector current and the collector-base reverse bias due to the space-charge region modulation in the lightly doped collector. To obtain $R_C(\text{sat})$, we analyze the expression for $V_{CE}(\text{sat})$ given by

$$V_{CE}(\text{sat}) = \frac{kT}{q} \ln \left(\frac{1 + (I_C/I_B)(1 - \alpha_R)}{\alpha_R (1 - (I_C/\beta_F I_B))} \right) + I_E R_E + I_C R_C, \quad (4.1)$$

where α_R is the common-base reverse current gain, β_F is the common-emitter forward current gain, and the other parameters in (4.1) have their usual meanings. From (4.1), we can obtain $R_E + R_C$ by plotting $V_{CE}(\text{sat})$ as a function of I_C , provided that the first term remains current independent. The effect of the first term of (4.1) can be reduced using the forced beta method. In this method, we measure the I_B - V_{CE} plots for the several values of I_C . We then find ΔV_{CE} as the difference between two points on two different curves for the same

ratio $\beta = I_C/I_B$. If we further assume that α_R and β_F are independent of I_C , and that $R_E \ll R_C$, then from (4.1) $R_C = \Delta V_{CE}/\Delta I_C$.

A method which uses the parasitic p-n-p transistor of the integrated n-p-n transistor to measure R_C was proposed [48]. At high currents, the collector current induces forward bias at the collector-base junction of the n-p-n transistor due to the voltage drop on the collector series resistance. The forward-biased collector-base junction of the n-p-n transistor behaves as the emitter of the p-n-p transistor. The holes injected into the epi that cross the subcollector are collected by the substrate and constitute a substrate current, I_S .

Since the base of the p-n-p is distributed across R_{CV} (Fig. 4.1), the question is where to attach the base terminal for the purpose of calculating the base-collector potential that controls I_S . Based on numerically calculated field profile in the epi, the base terminal of the p-n-p transistor was positioned at the epi-subcollector interface in the reference [48]. As will be shown later, the creation of the base terminal like this causes an error in determining of R_C from I_S . We also show that I_S is controlled directly by the physical base-collector junction of the n-p-n transistor.

For accurate modeling of a bipolar transistor, the two components of R_C (R_{CV} and R_{CY}) have to be separated and their bias dependence has to be determined. Neither of the above methods can do that. Our new method clearly separates the two components, and also yields their bias dependence. In addition, a new procedure for

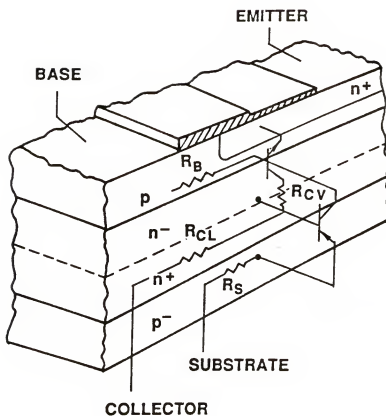
separating R_E from R_C using the forced beta method will be presented.

4.3 Physical Model

A careful investigation of the cross-section of the integrated n-p-n transistor reveals the presence of a parasitic p-n-p transistor, as shown in Figs. 4.2 (a) and 4.3 (a). In these figures, R_{CL} represents the resistance from the collector contact to the collector-substrate junction, and R_{CV} is resistance of the quasi-neutral epitaxial layer. The parasitic p-n-p transistor can be turned on by the voltage drop on the collector resistance of the n-p-n transistor. The emitter of the p-n-p transistor can be either the base or the substrate of the n-p-n transistor, depending on bias conditions. We define the upward operation of the p-n-p transistor, when the substrate-collector junction of the n-p-n transistor is forward biased, and the downward operation when the base-collector junction of the n-p-n transistor is forward biased.

4.3.1 Upward Operation of the p-n-p Transistor

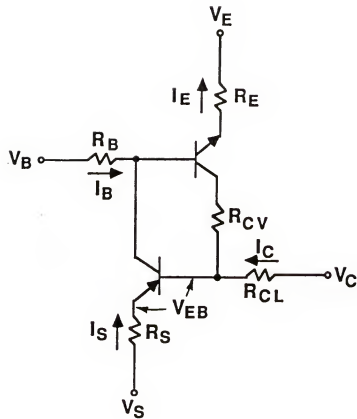
If the reverse bias at the collector-base junction is larger than the voltage drop on the R_{CL} and R_{CV} , the collector-base junction cannot turn on. Under this condition, however, the substrate-collector junction can turn on due to the voltage drop on R_{CL} . The substrate operates then as the emitter of the p-n-p transistor. Since the carrier injection into the base of the p-n-p transistor occurs at the substrate-collector junction in this



(a)

Fig. 4.2 Illustration of upward operation of the parasitic p-n-p transistor.

- (a) Device cross-section for upward operation of the parasitic p-n-p transistor. R_{CV} is the resistance of the n epi-layer, R_{CV} is the resistance of the n⁺ subcollector and plug.
- (b) Equivalent circuit for upward operation of the parasitic p-n-p transistor.



(b)

Fig. 4.2 (continued)

operation, the emitter current of the p-n-p transistor is controlled by the effective emitter-base junction voltage (V_{EB}) of the p-n-p transistor determined by the substrate and collector terminal voltage minus the voltage drop on R_{CL} (see Fig. 4.2 (a)).

For detailed analysis, we show the equivalent circuit for the upward operation of the p-n-p transistor in Fig. 4.2 (b). We assume that the R_{CL} is independent on the current levels, because the buried layer is usually heavily-doped. The voltage drop at the R_S is negligible in comparison with other components if the R_{CL} is obtained at the relatively low substrate current, for example, $I_S \leq 1 \mu A$. Then, V_{EB} of p-n-p for two different substrate voltage (V_S), is expressed as

$$V_{EB1} = V_{S1} - I_{S1}R_S + I_{C1}R_{CL} - V_C \quad (4.2)$$

$$V_{EB2} = V_{S2} - I_{S2}R_S + I_{C2}R_{CL} - V_C. \quad (4.3)$$

For the same I_S , V_{EB} will be the same. Thus, equaling (4.2) and (4.3) gives

$$R_{CL} = \frac{V_{S2} - V_{S1}}{I_{C1} - I_{C2}}. \quad (4.4)$$

The R_{CL} component of R_C is found uniquely from (4.4). This is a great advantage in comparison with other methods where different components of the series resistances are always coupled together.

4.3.2 Downward Operation of the p-n-p Transistor

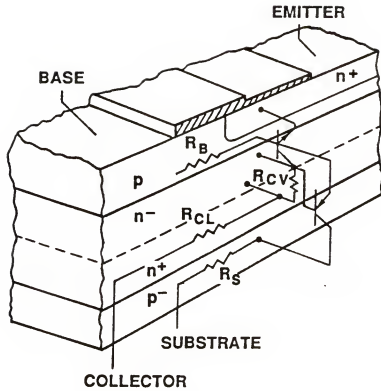
For the downward operation of the p-n-p transistor, the base-collector junction is forward-biased, while the substrate-collector junction is reverse-biased. Then, the potential right below the collector-base junction controls the emitter current of the p-n-p transistor, because the injection occurs at this junction. Thus, the base, collector, and substrate of the n-p-n transistor will behave as the emitter, base, and collector of the p-n-p transistor, as shown in Figs. 4.3 (a) and 4.3 (b). The holes injected from the p⁺ base transverse through the epitaxial layer and the subcollector and constitute the collector current of the p-n-p transistor. This current is also the substrate current of the n-p-n transistor (see Fig. 4.3 (b)). The collector current of the p-n-p transistor is controlled by the potential V_{EB} at top p-n junction determined by the terminal voltages V_B and V_C minus the voltage drop on both R_{CL} and R_{CV} :

$$V_{EB1} = V_B - R_{B1}I_{B1} + R_{C1}I_{C1} - V_{C1} \quad (4.5)$$

$$V_{EB2} = V_B - R_{B2}I_{B2} + R_{C2}I_{C2} - V_{C2}, \quad (4.6)$$

where the subscripts 1 and 2 correspond to V_{C1} and V_{C2} , respectively. The collector current of a transistor remains fixed when V_{EB} and V_{CB} are fixed. Thus, for the same I_S , V_{EB} in (4.5) and (4.6) will be the same:

$$R_C = R_{CV} + R_{CL} = \frac{V_{C1} - V_{C2}}{I_{C1} - I_{C2}} = \frac{\Delta V_C}{\Delta I_C}. \quad (4.7)$$

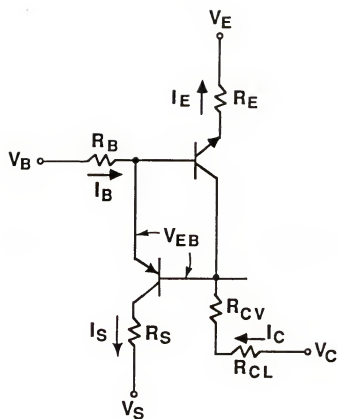


(a)

Fig. 4.3 Illustration of the downward operation of the parasitic p-n-p transistor.

(a) Cross-section for downward operation of the parasitic p-n-p transistor.

(b) Equivalent circuit for the downward operation of the parasitic p-n-p transistor.



(b)

Fig. 4.3 (continued)

Two assumptions were used in (4.7). The first assumption is that the voltage drop on the base resistance for two different values of V_C is almost the same. This assumption can be verified experimentally. For example, the voltage difference ($I_{B1}R_{B1} - I_{B2}R_{B2}$) for the transistor with the emitter size of $2 \times 12 \mu\text{m}^2$ is only about 2 mV for $\Delta V_C = 30$ mV. The second assumption is that R_C is constant for small variation of V_C ($\Delta V_C \leq 50$ mV). The small variation of V_C may modulate the base width of the p-n-p transistor, but this modulation is negligible for small ΔV_C .

In one previous work [48], the potential controlling I_S was chosen to be at the epi-subcollector junction. This corresponds to replacing R_C in (4.5) and (4.6) by R_{CL} . This neglects the voltage drop on R_{CY} . We show in the next section, that the value obtained for the downward operation mode includes R_{CY} .

4.4 Experimental Results

4.4.1 Measurement of the Collector Resistance

The measurements were performed on advanced self-aligned polysilicon-contact transistors. Figure 4.4 shows the current-voltage characteristics for transistor with the emitter mask size of $1.75 \times 4.75 \mu\text{m}^2$. Figure 4.5 shows the I_C and I_S versus V_{BE} curves for this transistor. The measurements were done for fixed $V_B = 0$ V and $V_C = 1$ V, while V_S was stepped by $\Delta V_S = 30$ mV from $V_S = 1$ V. The polarity of I_S is positive (I_S flows into the substrate), which confirms that the bottom p-n junction is forward-biased. Using the $I_S - V_{BE}$ curves, we find, for the same value of I_S , ΔI_C

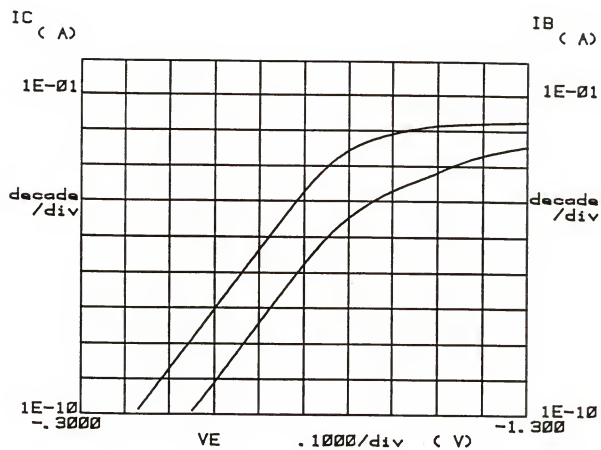


Fig. 4.4 Gummel plots for the transistor with the emitter mask size $A_{BE} = 1.75 \times 4.75 \mu\text{m}^2$. ($V_{BC} = 0$ V)

corresponding to ΔV_S shown in Fig. 4.5. Then, $R_{CL} = \Delta V_S / \Delta I_C$ from (4.4). Figure 4.6 shows the measured values for R_{CL} as a function of V_{BE} for three transistors with the emitter mask sizes of $1.75 \times 4.75 \mu\text{m}^2$, $1.75 \times 8 \mu\text{m}^2$, and $3 \times 8 \mu\text{m}^2$, respectively. As expected, R_{CL} is almost constant in the range from $V_{BE} = 0.9 \text{ V}$ to 1.1 V . We note, that R_{CL} for $1.75 \times 8 \mu\text{m}^2$ is larger than that for $3 \times 8 \mu\text{m}^2$. This can be explained in the following way. The collector current flows laterally through the buried layer in the extrinsic region of the transistor. But, the current flows mostly vertically in the buried layer under the intrinsic transistor area. The transistor with the larger emitter size will have the smaller contribution to R_{CL} from the intrinsic buried layer in comparison with the smaller emitter transistor, because the resistance is inversely proportional to the area perpendicular to the current flow. Thus, even if the spacing between the collector contact and the intrinsic region of the transistors is the same, they can have different R_{CL} due to the reason mentioned above.

The measured curves for the downward operation of the p-n-p transistor are shown in Fig. 4.7. The collector-substrate junction is reverse-biased with $V_S = -1 \text{ V}$, and $V_B = 0 \text{ V}$. We measure I_C and I_S as a function of V_{BE} for two different values of $V_C = -0.285 \text{ V}$ and -0.315 V . Because I_C is a strong function of the base width, the base-width modulation for ΔV_C should be considered. The base of the parasitic p-n-p consists of the epitaxial layer and the buried layer with total base-width of about $0.6 \mu\text{m}$. Thus, the base-width modulation for small $\Delta V_C \approx 30 \text{ mV}$ is negligible. This fact is

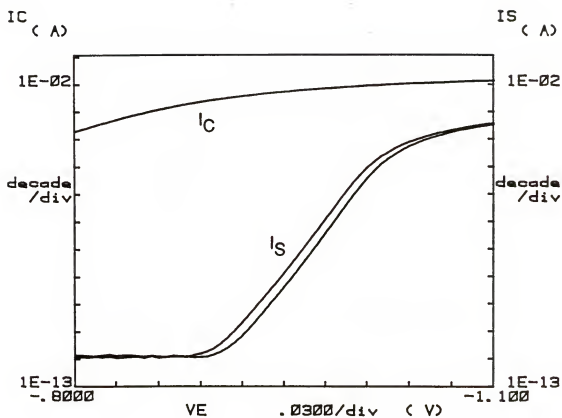


Fig. 4.5 I_C and I_S as a function of V_{BE} for transistor with $A_{BE} = 1.75 \times 4.75 \mu\text{m}^2$. The bottom I_S is for $V_S = 1$ V, the upper I_S curve is for $V_S = 1.03$ V.

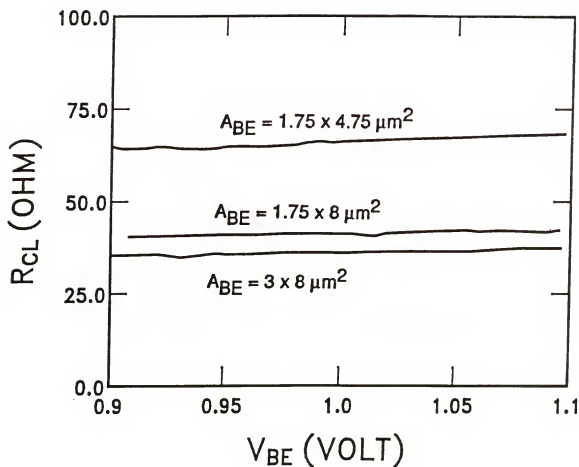


Fig. 4.6 Lateral collector series resistances for three different transistors as a function of V_{BE} . A_{BE} represents the emitter mask size.

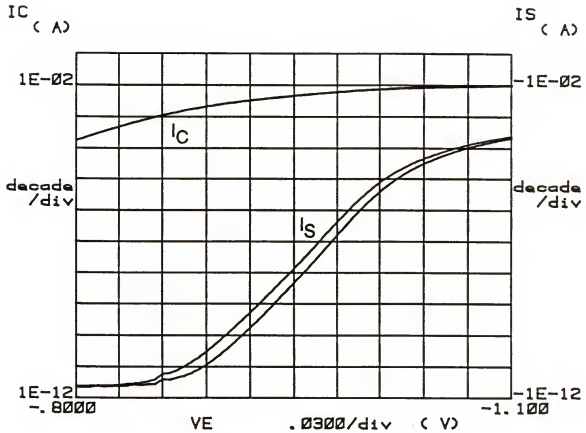


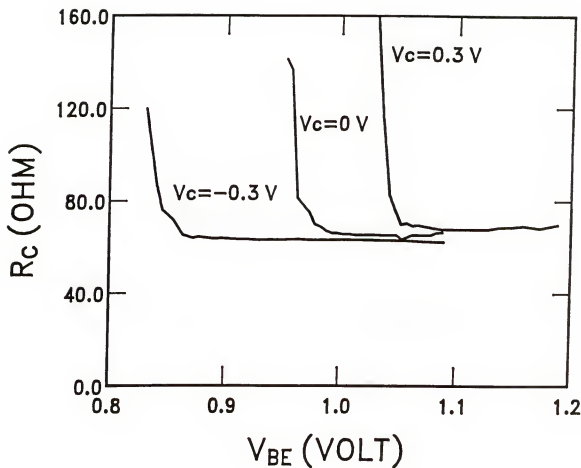
Fig. 4.7 I_C and I_S for the transistor with $A_{BE} = 1.75 \times 4.75 \mu\text{m}^2$ versus V_{BE} . Measurement conditions are $V_B = 0 \text{ V}$, $V_S = -1 \text{ V}$, $V_C = -0.285 \text{ V}$ for the top I_S curve, and $V_C = -0.315 \text{ V}$ for bottom I_S curve.

confirmed by the fact that the $I_C - V_{BE}$ curves in Fig. 4.7 for both values of V_C are nearly identical. The total collector resistance $R_C = R_{CV} + R_{CL}$ is obtained from Fig. 4.7 in a similar way as for the previous case of the upward operation by measuring ΔI_C corresponding to ΔV_C , and then using (4.7).

To investigate the R_C dependence for $V_{BE} \leq 0.9$ V, the current offset (≈ 1 pA) can be subtracted from the I_S values measured for higher biases. It is not easy to measure I_S in the pA range due to the leakage current between the leads of the package. Cleaning the package and the plug-in of the shielded box of the HP4145 analyzer with alcohol dramatically reduces the leakage currents. To obtain the flat offset currents of I_S , the hold-time of HP4145 was set to 20 seconds.

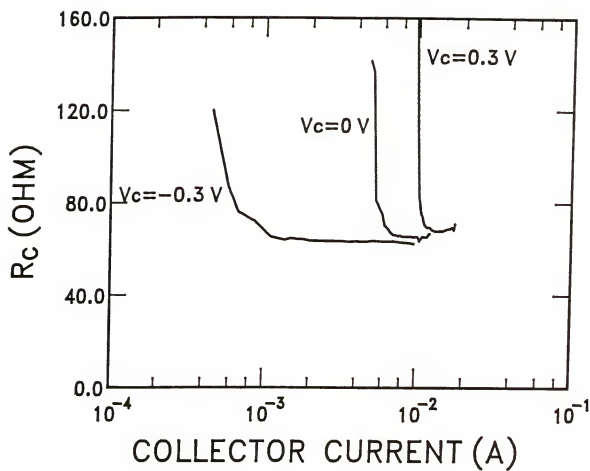
The measured dependencies of R_C on V_{BE} and I_C for two transistors are shown in Figs. 4.8 (a) and (b) and in Fig. 4.9. At high currents, R_C saturates at $R_C = R_{CL}$, which agrees very well with the R_{CL} dependence found in Fig. 4.6. For smaller currents, R_C sharply increases because of the contribution from the epitaxial layer of R_{CV} . The very sharp transition from the low-current value to the high-current value is caused by the conductivity modulation of the epitaxial layer.

To investigate the dependence of R_C on bias in more physical detail, we performed numerical simulations using MEDUSA simulator. Figs. 4.10 (a) and (b) show the simulated dependence of R_C on V_{BE} and I_C for $V_C = -0.3$ V for a transistor with $1.75 \times 4.75 \mu\text{m}^2$ emitter size. The doping profiles and geometry for the simulated



(a)

Fig. 4.8 Total collector resistances versus (a) V_{BE} and (b) I_C for three different values of V_C . $A_{BE} = 1.75 \times 4.75 \mu\text{m}^2$, $V_S = -1 \text{ V}$.



(b)

Fig. 4.8 (continued)

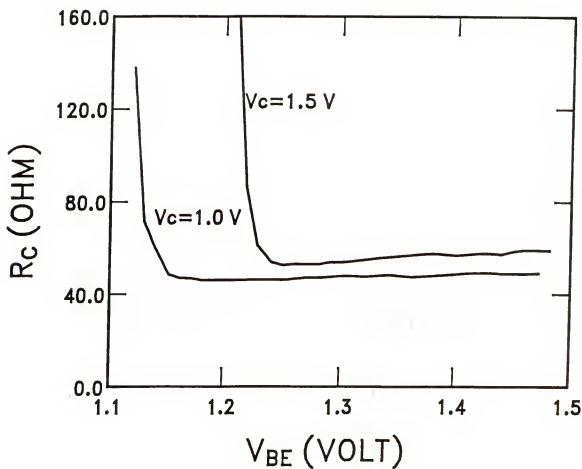


Fig. 4.9 Total collector resistance versus V_{BE} for two different values of V_C . $A_{BE} = 1.75 \times 8 \mu\text{m}^2$, $V_S = -1$ V, 1.5 V.

transistor are similar to that measured in Fig. 4.8. The qualitative agreement between Figs. 4.8 and 4.10 is excellent.

R_C in Fig. 4.10 is calculated from the quasi-Fermi potential difference between the collector contact and the edge of the base-collector space-charge region. The boundary between the quasi-neutral collector and the base-collector space-charge region is rather easy to determine at small and moderate biases from the electric field profile. This gets more difficult at biases where the quasi-neutral base pushes out into the epi region and the electron concentration is comparable or larger than the collector donor concentration. It is easier to approximate the boundary by using the difference between the electron and doping concentrations and identify the boundary at a position at which $n = N_D$. This criterion was used to calculate R_C displayed in Fig. 4.10.

Figure 4.11 shows the detailed simulated dependencies of the excess electron concentration, electric field, and R_C on the distance from the emitter surface for $V_{BE} = 0.87$ V ($I_C = 0.82$ mA). R_C is measured from the collector contact. Also shown is the $\log n - \log N_D$ curve. Note that $n = N_D$ for $x \approx 0.52$ μm where $R_C \approx 203$ Ω . For small currents, R_C is almost constant and equal to R_{CV} . At $V_{BE} \approx 0.87$ V, the injected electron concentration approaches the doping in the epi layer (see Fig. 4.11). As a result, R_{CV} (and R_C) rapidly drops, as shown in Fig. 4.10 (a). Simulation shows that for $V_{BE} \geq 0.89$ V, $n > N_D$, and, hence, R_C drops to a low value of $R_C \approx R_{CL}$.

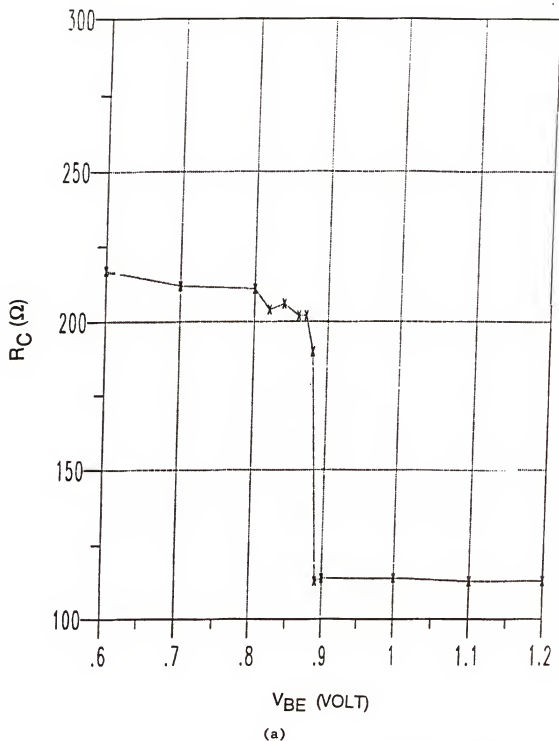
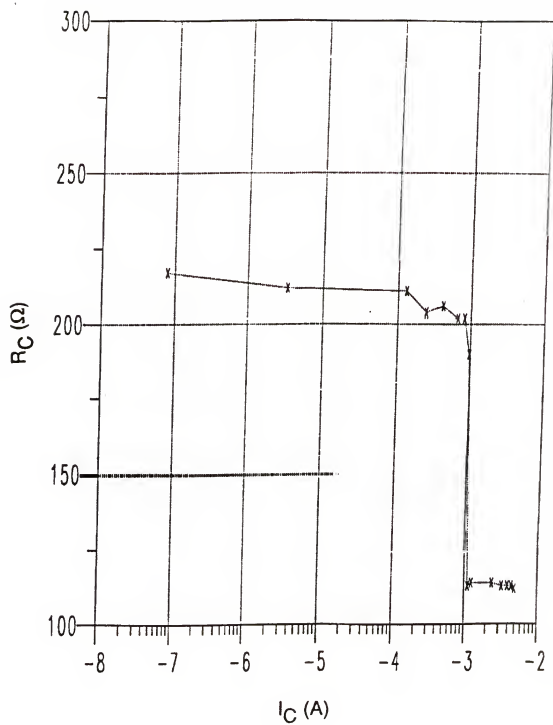


Fig. 4.10 Simulated total collector resistance from MEDUSA versus
(a) V_{BE} and (b) I_C for the transistor with $A_{BE} = 1.75 \times 4.75 \mu\text{m}^2$.



(b)

Fig. 4.10 (continue)

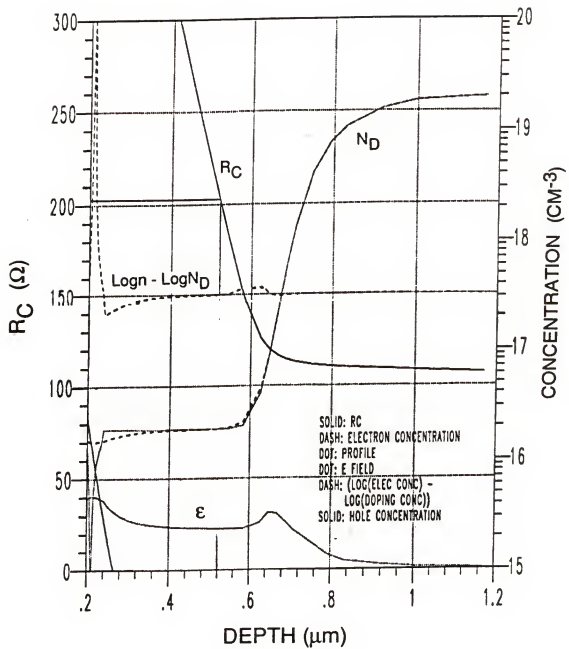


Fig. 4.11 Simulation results from MEDUSA for $V_{BE} = 0.87$ V, $V_{BC} = -0.3$ V, $A_{BE} = 1.75 \times 4.75 \mu m^2$.

The sharp transition between the low-current and high-current values of R_C shown in Figs. 4.8 and 4.9 strongly depends on the external collector bias V_C . The internal base-collector potential is given by the external voltages V_C and V_B minus the voltage drop on the collector resistance. As V_C in Fig. 4.8 (a) changes from, for example, 0 V to + 0.3 V, the base-collector junction becomes more reverse-biased. Thus, it takes larger I_C to induce enough voltage drop $R_C I_C$ to forward bias the junction. The critical collector current for the onset of the base push-out also increases with the increasing base-collector reverse bias in ohmic saturation and quasi saturation [11-12]. The transition between the low- and high- R_C is, thus, moved to higher currents as V_C increases (Fig. 4.8(b)). Since the collector resistance after the onset of the base push-out is a strong function of the high injection, it is not easy to clearly explain the values for the plateau in Fig. 4.8.

4.4.2 Measurement of the Emitter Resistance

As discussed in Section 4.2, the slope of the $I_C - V_{CE}$ curve in saturation is proportional to the sum $R_{CL} + R_E$. As the device size gets smaller, R_E becomes larger because R_E is inversely proportional to the emitter area, also becomes smaller due to the shorter distance from the collector contact to the intrinsic collector-base junction. Nevertheless, R_E may become comparable to R_{CL} . A very accurate value for R_{CL} can be obtained from I_S of the upward operation mode of the p-n-p transistor, as was described above.

Below we describe a new method for extraction of R_E based on measurement of R_{CL} combined with the forced beta method.

Before describing the detailed procedure, we point out the problem encountered during the measurement of $R_C(\text{sat}) + (1 + 1/\beta)R_E$ by taking the slope of the I_C - V_{CE} plot. We found that the slope varies in a wide range. For example, for the transistor with the emitter size of $1.75 \times 4.75 \mu\text{m}^2$ the slope varies in between 68 Ω and 81 Ω , depending on the points at which the slopes are taken. The reason for the various slopes is that the internal saturation voltage $V_{CE}(\text{sat})$ is not negligible in comparison with $R_C(\text{sat}) + (1 + 1/\beta)R_E$.

Thus, we chose the forced beta method that overcomes the problem with the variable slope. For I_C/I_B fixed, we derive from (4.1)

$$\frac{\Delta V_{CE}}{\Delta I_C} = R_C(\text{sat}) + \left(1 + \frac{\Delta I_B}{\Delta I_C}\right) R_E. \quad (4.11)$$

The sum of the collector and emitter resistances can be obtained accurately from (4.11). This method is usually used to measure $R_C(\text{sat})$ by either neglecting R_E or estimating R_E by the open-collector method [24]. It was shown [27], however, that the open-collector method is not reliable and grossly overestimates R_E . We can use (4.11) to extract R_E , provided that $R_C(\text{sat})$ can be measured independently and accurately. Under the heavily saturated operating conditions $R_C(\text{sat}) \approx R_{CL}$, which can be independently measured from the upward mode of the p-n-p transistor.

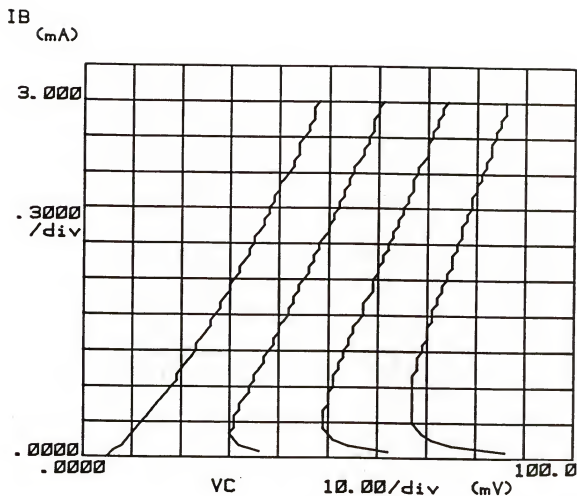


Fig. 4.12 I_B versus V_C with I_C as a parameter for transistor with $A_{BE} = 1.75 \times 4.75 \mu\text{m}^2$. The collector currents are from left to right: 0 mA, 0.2 mA, 0.4 mA, and 0.6 mA.

In Fig. 4.12, we illustrate a typical $I_B - V_{CE}(\text{sat})$ plot for the transistor with the emitter mask size of $1.75 \times 4.75 \mu\text{m}^2$. We investigated the variation of $\Delta V_{CE}/\Delta I_C$ as function of current. The results are summarized in Table 4.1 calculated from (4.11) and using the R_{CL} data from Fig. 4.6 together with the values for R_E . The variation of R_E is within 10 %. Although R_{CL} is about six times larger than R_E , the two terms in (4.11) are about the same since $\Delta I_B/\Delta I_C \approx 4-6$ (see Table 4.11). The accuracy of the extracted value for R_E depends on the accuracy of R_{CL} . The new method presented here is sufficiently accurate for this purpose. The values for R_E for three transistors are summarized in Table 4.2. By subtracting $0.4 \mu\text{m}$ wide sidewall from the emitter mask size, we obtain the effective emitter area. From the effective emitter area and the values for R_E from Table 4.2, we obtain the average value for the specific contact resistivity of $\rho_C \approx 50 \Omega\text{-}\mu\text{m}^2$.

4.5 Conclusions

New DC methods to measure the collector resistance R_C and emitter resistance R_E of integrated-circuit bipolar transistors are presented. The method for R_C is based on monitoring the substrate current of the parasitic p-n-p transistor linked with the n-p-n intrinsic transistor. The p-n-p transistor is operated with either the bottom or top p-n junction forward-biased. This allows to separate the two components of R_C . R_E is obtained from the measured lateral portion of R_C and collector-emitter saturation voltage.

Table 4.1 Dependence of R_E on I_C for the transistor with the emitter mask size of $1.75 \times 4.75 \mu\text{m}^2$.
 R_E was obtained from (4.8) using $R_{CL} = 64 \Omega$ from Fig. 4.6.

I_C (mA)	I_B (mA)	V_{CE} (mV)	$\Delta V_{CE} / \Delta I_C$ (Ω)	R_E (Ω)
0.2	0.9	38	130	12
0.3	1.35	51		
0.2	0.8	36	120	11.2
0.4	1.6	60		
0.2	1	38	130	11
0.4	2	64		
0.2	1.2	41	135	10.14
0.4	2.4	68		

Table 4.2 Summary of R_E for three emitter mask sizes.

A_{BE} (μm^2)	R_{CL} (Ω)	R_E (Ω)
1.75 x 4.75	64	11 ~ 12
1.75 x 8	41	7 ~ 7.58
3 x 8	37	4 ~ 4.5

Examples of measurements on advanced self-aligned transistors with polysilicon contacts are shown and compared with numerical simulations. The results show very strong dependence of R_C on the base-emitter and base-collector voltages of the n-p-n transistor. The bias dependence of R_C is due to the conductivity modulation of the epitaxial collector. From the measured R_E we obtain a value for the specific contact resistance for the polysilicon emitter contact of $\rho_C \approx 50 \text{ } \Omega\text{-}\mu\text{m}^2$.

CHAPTER FIVE MEASUREMENTS OF THE AUGER COEFFICIENTS

5.1 Introduction

There are large discrepancies of the Ambipolar Auger coefficients $C_A = C_n + C_p$ from one investigator to another. The values from Dziewior and Schmid [49] and Svantesson and Nilsson [50] for the plasma density of above $1 \times 10^{18} \text{ cm}^{-3}$ ($3.8 \times 10^{-31} - 3.4 \times 10^{-31} \text{ cm}^6\text{s}^{-1}$) are almost same. Dziewior and Schmid extracted the carrier lifetime from the decay time of the band-to-band recombination radiation after pulsed excitation by a mode-locked cavity-dumped Ar^+ -ion laser. Svantesson and Nilsson used almost the same method except for measuring the recombination radiation in a direction perpendicular to the laser beam (YAG:Nd). The absorption of infrared probe radiation by nonequilibrium carriers, excited with light from a Neodymium laser, was used to measure C_A [51]. The value for C_A from this experiment is $1.5 \times 10^{-30} \text{ cm}^6\text{s}^{-1}$ for the plasma density above $5 \times 10^{17} \text{ cm}^{-3}$. The C_A from the photo-conductivity and the dynamic grating experiment is $1.1 \times 10^{-30} \text{ cm}^6\text{s}^{-1}$ for the plasma density below $1 \times 10^{18} \text{ cm}^{-3}$ [52]. In the experiments based on measuring the lifetime, the surface recombination of the sample is always a problem.

Two approaches to solve this problem, by a chemical preparation method [53] or by growing good quality oxide layer on the surface of the device [54] were reported. A strobe lamp excites carriers in a

semiconductor wafer immersed in hydrofluoric acid, and their density decay is then monitored by an inductively coupled rf bridge [53]. The value from this measurement is $2 \times 10^{-30} \text{ cm}^6\text{s}^{-1}$ for the plasma density in the range of 3×10^{15} to 10^{17} cm^{-3} . By monitoring the open-circuit voltage of a highly injected solar cell under steady-state and transient conditions, the C_A was extracted [54]. The value reported from this experiment is $1.66 \times 10^{-30} \text{ cm}^6\text{s}^{-1}$ for the plasma densities in the range of 1×10^{16} to $1.2 \times 10^{17} \text{ cm}^{-3}$.

In this chapter, we present measurements of Auger lifetime in the carrier density range from 10^{17} to $5 \times 10^{17} \text{ cm}^{-3}$. Our experimental method is fundamentally different from other methods [49-54], since we measure the electroluminescence (EL) as a function of the current through a $n^+/p^-/p^+$ diode. To extract the Auger recombination coefficient, the experimental results are compared with numerical calculations that self-consistently solve the transport equations across the p^- base of the diode. The connection between experimental and numerical results is made possible by normalizing the electroluminescence signal at high currents with respect to the same signal under low injection. For carrier plasma densities between 10^{16} and 10^{17} cm^{-3} , recombination in the n^+ and p^+ layer dominates the current and the relation between electroluminescence and current is linear. In this density range, fitting experimental results with numerical calculations reveals the saturation current density of the heavily doped regions. For plasma densities between 10^{17} and $5 \times 10^{17} \text{ cm}^{-3}$, Auger recombination reduces the base ambipolar lifetime well below its Shockley-Read-

Hall value. The base recombination becomes comparable to the recombination in the heavily doped regions and the electroluminescence intensity starts increasing sublinearly with the current. The Auger coefficient is extracted as a fitting parameter in the numerical solutions that simulate the experimental sublinearity.

The section that follows presents the experimental method, results and the extraction of parameters based on numerical solutions. In section Section 5.3, we discuss the sensitivity and accuracy of the method and provide experimental evidence for certain assumptions used in the interpretation of the experimental results. In the conclusion section, the main points of the paper are summarized.

5.2 Experimental Results and Numerical Interpretation

The device under study has the $n^+/p^-/p^+$ structure cut from a high efficient solar cell. The p^- layer has the doping concentration N_A of $1.2 \times 10^{15} \text{ cm}^{-3}$ and the width W of $100 \text{ }\mu\text{m}$. The device is mounted on T0-5 package and bonded with 16 bonding wires for each electrode. The bonded device was attached to the heat radiator for the possible heat-up of the device during the high injection period. The device temperature was monitored through the thermocouple mounted on the heat radiator. We applied the forward bias to the diode in the pulse mode to prevent it from heating up, as shown in Fig. 5.1. The repetition rates of the pulse span in the $0.3 \text{ Hz} - 100 \text{ Hz}$ range depending on the current levels. The pulse with the 10^{-5}

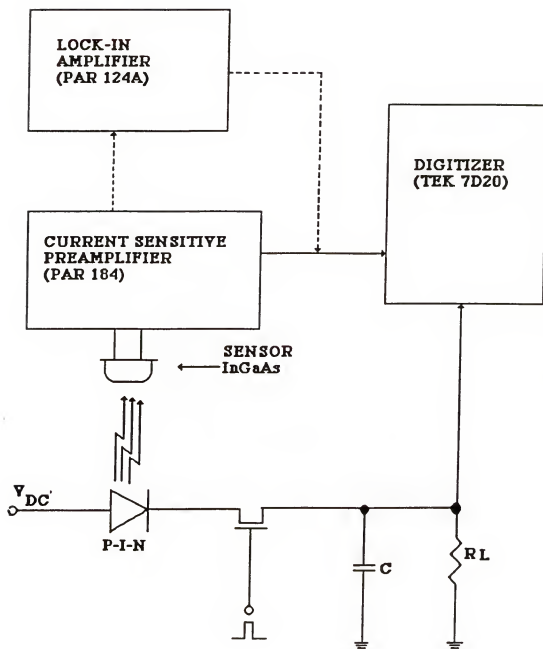


Fig. 5.1 Schematic illustration of the experimental setup for measurement of the electroluminescence versus current for p-i-n diode. MOS switch is IRF510. R_L is 0.2 Ω or 52 Ω depending on the current levels.

duty cycle of 3 sec period was used especially at the high current density ($J \geq 1.5 \times 10^3 \text{ A/cm}^2$). The electroluminescence signal was detected by InGaAs photodetector. The detected signal was amplified by the current sensitive amplifier (PAR 184) for large signals or amplified again by the lock-in amplifier (PAR 124A) for the weak signal from low currents (see the dashed sequence in Fig. 5.1).

Figure 5.2 shows how the experimental electroluminescence signal, EL as a function of the terminal current, I . The plot has three distinct regions. In region 1, EL is a superlinear function of I , while EL depends linearly on I in region 2. In region 3, the electroluminescence signal is a sublinear function of I and, as discussed later, it is this region that is the most sensitive to the ambipolar Auger recombination in the base. To understand how EL depends on I , we can introduce an approximate model about the carrier transport in the base and assume that the carrier plasma density is uniform throughout the quasi-neutral base. Accurate numerical results that allow a more precise parameter extraction will be presented later in Section 5.2.2.

5.2.1 Approximate Analytical Model

In this approximate model, let n be the uniform electron-hole density in the base that corresponds to the terminal current I . The density of electrons and holes can be assumed to be equal for carrier injection levels above 10^{16} cm^{-3} . Let J_{on} and J_{op} be the saturation current densities of the n^+ and p^+ regions, respectively, let τ_{SRH} be the Shockley-Read-Hall (SRH) ambipolar base lifetime and

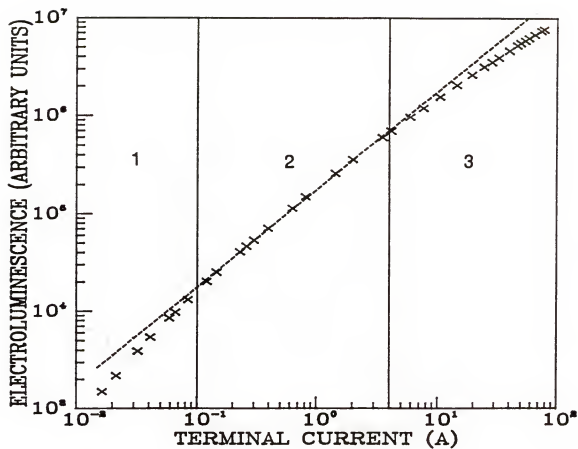


Fig. 5.2 Measured electroluminescence versus current through the p-i-n diode.

C_A be the ambipolar Auger coefficient in the base. For carrier densities high enough so that we can neglect the recombination in the space charge region of the base emitter junction as well as recombination at the lateral edge, the current as a function of n takes the form

$$I = A(J_{on} + J_{op})n^2/n_i^2 + eAWn/\tau_{SRH} + eAWC_A n^3, \quad (5.1)$$

where A is the area of the device, W is width of the p^- base, and J_{on} and J_{op} are recombination currents in heavily doped n^+ and p^+ , respectively.

To be able to judge the relative weight of the three terms in (5.1), we can use values for the recombination parameters that are usually adopted in the literature. The sum $J_{on} + J_{op}$ is of the order of 10^{-12} A/cm², the high injection SRH lifetime is usually more than 100 μ s in solar cell grade material, and the reported values of C_A are in the range from 0.4×10^{-30} to 2×10^{-30} cm⁶s⁻¹ [49-54]. Therefore, in (5.1) the first term dominates when n varies between 10^{16} and 10^{17} cm⁻³. Thus, in this range

$$I = A(J_{on} + J_{op})n^2/n_i^2. \quad (5.2)$$

At the same time, the electroluminescence signal is proportional to the integrated pn product in the base. If F is a proportionality constant then

$$EL = Fn^2. \quad (5.3)$$

From (5.2) and (5.3)

$$EL = F \frac{n_i^2 I}{(J_{on} + J_{op})A} \quad (5.4)$$

and, therefore, in the range from 10^{16} to 10^{17} cm^{-3} EL is a linear function of I . This range roughly corresponds to region 2 in Fig. 5.2.

For densities above 10^{17} cm^{-3} , the Auger term in (5.1) becomes important and now

$$I = A(J_{on} + J_{op})n^2/n_i^2 + eAWC_A n^3 \quad (5.5 \text{ a})$$

$$I = A(J_{on} + J_{op})EL/(Fn_i^2) + eAWC_A(EL/F)^{3/2}. \quad (5.5 \text{ b})$$

Equation (5.5 b) implies that for carrier densities above 10^{17} cm^{-3} the electroluminescence increases sublinearly with I and this correspond to region 3 in Fig. 5.2. Region 1 corresponds to carrier densities below 10^{16} cm^{-3} , where (5.1) becomes

$$I = A(J_{on} + J_{op})n^2/n_i^2 + eAWn/\tau_{SRH} \quad (5.6 \text{ a})$$

$$I = A(J_{on} + J_{op})EL/(Fn_i^2) + eAW(EL/F)^{1/2}/\tau_{SRH} \quad (5.6 \text{ b})$$

which implies a superlinear dependence of EL on I . To this superlinear dependence also contributes the recombination current in the space charge region of the emitter junction as well as the recombination current at the lateral surface of the diode. This is the case since these currents depend on n according to n^α , where α is in the vicinity of 1.

The above arguments would be more convincing if we could independently calculate the average carrier density as a function of the current and verify that the demarcation levels between regions 1, 2, and 3 correspond to carrier densities in the vicinity of 10^{16} and 10^{17} cm^{-3} . Here, by average carrier density we mean the rms value of the pn product in the base. This carrier density, n , can be calculated from (5.3) provided that EL can be measured at a bias level where n is known. Low injection can serve as such a bias level since, under the uniform carrier density approximation,

$$EL_0 = F n_0^2 = F n_1^2 \exp(eV_0/kT), \quad (5.7)$$

where V_0 is the terminal voltage. In low injection the current is low enough to eliminate any series resistance voltage drop, so that (5.7) holds. In Fig. 5.3, we plot EL_0 as a function of the terminal voltage in low injection. It can be seen that EL_0 changes according to (5.7) and, thus, series resistances effects are negligible. By combining (5.3) and (5.7) we obtain

$$n^2 = (EL/EL_0) n_1^2 \exp(eV_0/kT). \quad (5.8)$$

Therefore, by measuring EL at an injection level low enough so that (5.7) applies, we can calculate F . Knowledge of F allows calibrating the measurements at high current levels where, due to series resistance and high injection effects, the terminal voltage is not a useful parameter. From Fig. 5.2 and 5.3 and (5.8) the boundary between regions 1 and 2 in Fig. 5.2, corresponds to $n = 1.6 \times 10^{16} \text{ cm}^{-3}$ while the boundary between regions 2 and 3 corresponds

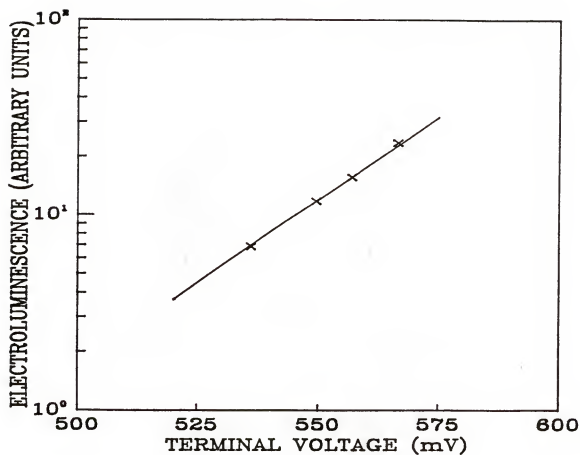


Fig. 5.3 Measured electroluminescence versus terminal voltage of the p-i-n diode at low current.

to $n = 9.8 \times 10^{16} \text{ cm}^{-3}$ in agreement with the previous calculations based on generally accepted recombination parameters. Equation (5.8) can, in addition to n , provide an approximate calculation for the sum $J_{\text{on}} + J_{\text{op}}$. From (5.2) and (5.8)

$$J_{\text{on}} + J_{\text{op}} = I/[A(EL/EL_0)\exp(eV_0/kT)] \quad (5.9)$$

where EL and I belong to region 2. From (5.9) and Fig. 5.2 and Fig. 5.3, $J_{\text{on}} + J_{\text{op}} \approx 8.7 \times 10^{-13} \text{ A/cm}^2$, in agreement with the original assumption about the sum $J_{\text{on}} + J_{\text{op}}$.

From the above discussion, and since $J_{\text{on}} + J_{\text{op}}$ is known, one might be attempted to calculate C_A from (5.5) and (5.8). However, as we point out later, for injection levels above 10^{17} cm^{-3} the carrier density is not uniform and the above approximations can lead to large errors. In order to derive more accurate values for J_{on} , J_{op} , and C_A , we will simulate the experimental results using numerical solutions for the carrier density across the quasi neutral base. The simulation will be restricted to the regions 2 and 3 because these regions, as explained above, are the most sensitive to J_{on} , J_{op} and C_A , and they are much more immune to parasitic currents than the region 1.

5.2.2 Numerical Analysis

To accurately simulate the experimental results, the transport equations were numerically and self-consistently solved from the n^+/p^- to the p^-/p^+ edge of the quasi neutral base. The transport equations are

$$J_n(x) = -q\mu_n n(x) \frac{d\phi_n}{dx} \quad (5.10 \text{ a})$$

$$J_p(x) = q\mu_p p(x) \frac{d\phi_p}{dx} \quad (5.10 \text{ b})$$

$$p(x) = N_A + n(x) \quad (5.10 \text{ c})$$

$$p(x)n(x) = n_i^2 \exp[q(\phi_p - \phi_n)/kT] \quad (5.10 \text{ d})$$

$$J_n(W) = \frac{n(W)p(W)}{n_i^2} J_{op} \quad (5.10 \text{ e})$$

$$J_p(0) = \frac{n(0)p(0)}{n_i^2} J_{on}. \quad (5.10 \text{ f})$$

The solution of these equation provides $n(x)$ and I . Since n is now a function of x equation (5.3) becomes

$$EL = \frac{F}{W} \int_0^W n^2(x) dx. \quad (5.11 \text{ a})$$

As we prove in appendix C, to include the free carrier absorption we must multiply the expression in (5.11 a) by following factor.

$$MF = 1 - \sigma \int_0^W n(x) dx. \quad (5.11 \text{ b})$$

$$\left(\ln \left(\frac{1}{\sigma \int_0^W n(x) dx} \right) + y - \ln(y) - \int_0^y \exp(-1/x) dx \right)$$

where σ is the absorption cross section of the electron hole plasma and y is arbitrary number much larger than 10. The free-carrier absorption factor is written here in terms of n , but this is of no consequence since it becomes important only if the carrier density is above 10^{17} cm^{-3} where $n(x)$ and $p(x)$ are essentially the same. Thus (5.11 a) becomes

$$EL = (F/W) \left(1 - MF \right) \int_0^W n^2(x) dx. \quad (5.11 c)$$

As in the previous subsection, the proportionality constant F is calculated from the voltage dependence of EL in low injection, which is shown in Fig. 5.3. Instead of the simplified expression in (5.7), we now take into account the minority carrier variation across the base. Since the base is uniform, closed-form expressions are available for the minority carrier density in the base, and now (5.7) becomes

$$EL_0 = F n_0^2 = F n_1^2 \exp(eV_0/kT) .$$

$$\frac{(L/W)[\sinh(W/L) + (SL/D)\cosh(W/L) - SL/D]}{\cosh(W/L) + (SL/D)\sinh(W/L)}. \quad (5.11 d)$$

In (5.11 d), S is the recombination velocity at the p^-/p^+ interface and L is the low injection diffusion length. Since in high quality solar cells SL/D is a small number and L can be several hundred microns, the large fraction in (5.11 d) is very close to 1. Thus (5.7) overestimates EL_0 by 5% to 10% only.

5.2.3 Extraction of J_{on} and J_{op}

To reduce the number of unknowns and calculate L and S required by (5.11 d) for the calculation of F , an independent experiment was done to calculate the low injection lifetime, τ , and S . The diode was excited by a uniformly absorbed pulse of a nanosecond NYAG laser ($\lambda = 1.064 \mu\text{m}$) and the short circuit current response was analyzed using the FDTA method [55]. The amplitude and phase response of the short circuit current are shown in Fig. 5.4 and Fig. 5.5, respectively. The low injection lifetime from this experiment was $\tau = 50 \pm 5 \mu\text{s}$ and the recombination velocity was $S = 26.5 \pm 5 \text{ cm/s}$. From (5.11 d) and Fig. 5.3, $F = 4.63 \times 10^{-29}$ (arb. units). The uncertainty in τ and S has negligible effects on F since, as already discussed, the big fraction in (5.11 d) is close to 1 and insensitive to $L \approx 420 \mu\text{m}$ and $SL/D \approx 0.032$. Knowledge of S allows calculation of J_{op} through the relation

$$J_{op} = eS n_i^2 / N_A = (4.4 \pm 0.9) \times 10^{-13} \text{ A/cm}^2. \quad (5.12)$$

Since J_{op} is independently known, fitting the experimental results in region 2 with the numerical solutions will yield J_{on} . As we demonstrate in the next section, any decrease in value of the mobilities in region 2, has no effect on the numerical solutions for the EL dependence on I , in the same region. In addition, the free-carrier absorption is not important for carrier densities below 10^{17} cm^{-3} . Therefore, J_{on} is essentially the only fitting parameter in region 2 and its value almost uniquely depends on the experimental

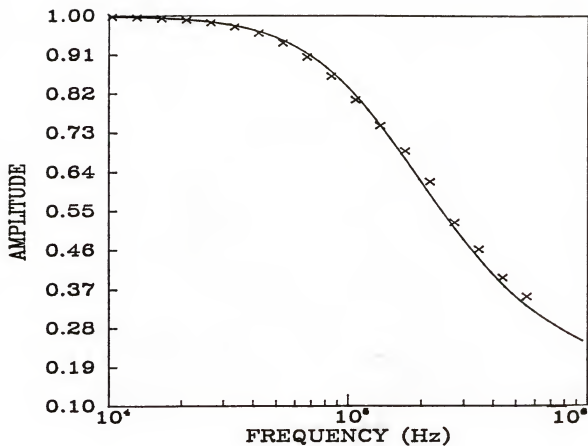


Fig. 5.4 Amplitude response from frequency-domain transient analysis for $n^+/p^-/p^+$ diode. The parameters for the best fit are $\tau = 50 \mu s$, $S = 26.5$ cm/sec.

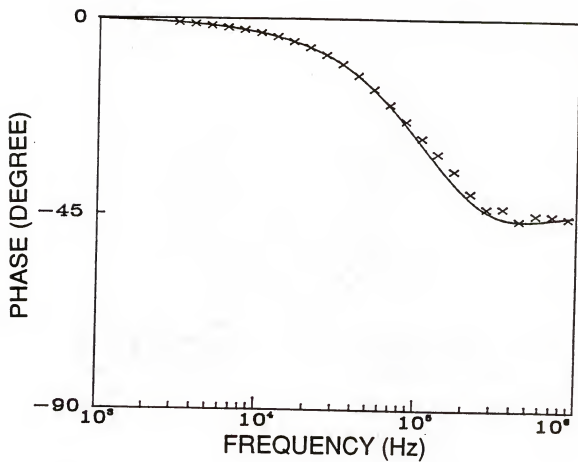


Fig. 5.5 Phase response from the frequency-domain transient analysis for $n^+/p^-/p^+$ diode. The parameters for the best fit are $\tau = 50 \mu\text{s}$, $S = 26.5 \text{ cm/sec}$.

results and J_{op} . When $J_{op} = 4.4 \times 10^{-13} \text{ A/cm}^2$, fitting in region 2 yields $J_{on} = 4.3 \times 10^{-13} \text{ A/cm}^2$. The variation of J_{op} in (5.12) induces a similar variation in J_{on} . The effects of these variations on the calculation of C_A will be discussed in the next section. Fitting in the vicinity between regions 1 and 2 yields the high injection SRH ambipolar lifetime $\tau_{SRH} = 150 \pm 20 \text{ } \mu\text{s}$. The uncertainty in this lifetime has negligible effects in the upper half of region 2 and almost no effect in region 3.

5.2.4 Extraction of C_A

C_A is obtained from the fitting in region 3. Here, the value of the mobilities and the value of σ do affect the numerical results. The variation of mobilities with carrier density was taken from the book by Baliga [56] while the value for σ was taken from data by Svantesson [57]. Svantesson measured σ at a wavelength of $1.064 \text{ } \mu\text{m}$ and found $\sigma = 5.1 \times 10^{-18} \text{ cm}^2$. The electroluminescence spectrum of silicon is sharply peaked at $1.1 \text{ } \mu\text{m}$ and, therefore, we can extrapolate the previous value of σ following the cubic law dependence of σ on the wavelength [58]. Doing so yields $\sigma = 5.64 \times 10^{-18} \text{ cm}^2$.

Using these values for the mobilities and σ and having already calculated J_{on} and J_{op} , the fitting in region 3 becomes a one parameter fit, C_A being the fitting parameter. C_A was changed by steps of $0.01 \times 10^{-30} \text{ cm}^6\text{s}^{-1}$. The best fit was obtained for $C_A = 1.77 \times 10^{-30} \text{ cm}^6\text{s}^{-1}$. Figure 5.6 shows the experimental and numerical results for a current variation over three orders of magnitude that

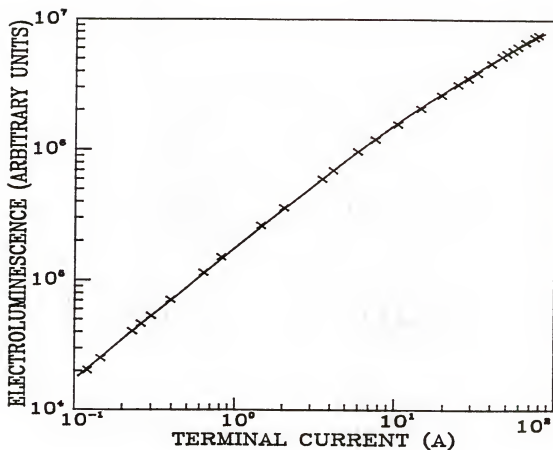


Fig. 5.6 Curve fitting based on numerical calculation.

The parameters for the best fit are $J_{on} = 4.3 \times 10^{-13}$ A/cm², $J_{op} = 4.4 \times 10^{-13}$ A/cm², and $C_A = 1.77 \times 10^{-30}$ cm⁶s⁻¹. Mobilities are from ref. [56].

covers regions 2 and 3. The overall agreement is better than 98%. Figure 5.7 emphasizes the high current region and demonstrates the sensitivity of the fitting to C_A . In Table 5.1 we summarize the values of the extracted parameters.

Table 5.1 Summary of the data set for the best fit.

J_{on}	J_{op}	τ_{SRH}	C_A
(10^{-13} A/cm ²)	(10^{-13} A/cm ²)	(μ s)	10^{-30} cm ⁶ s ⁻¹
4.3	4.4	150	1.77

5.3 Discussion

5.3.1 Sensitivity of C_A to other parameters

Figure 5.8 demonstrates the effect that changes in the mobilities have on the numerical calculations. We see that for currents in the region from 0.1 to 5 A, the numerical results are almost completely insensitive to any changes in the mobilities. Since this region is the same as region 2, we can safely conclude that the extraction of J_{on} does not depend on the exact knowledge of the mobilities.

Figure 5.9 (a) and Fig. 5.9 (b) show that the plasma densities in the p^- region for the cases of with and without the Auger recombination, respectively. We can see that the plasma densities at low currents are same for both cases. However, they are different at high currents. The plasma distributions without the Auger

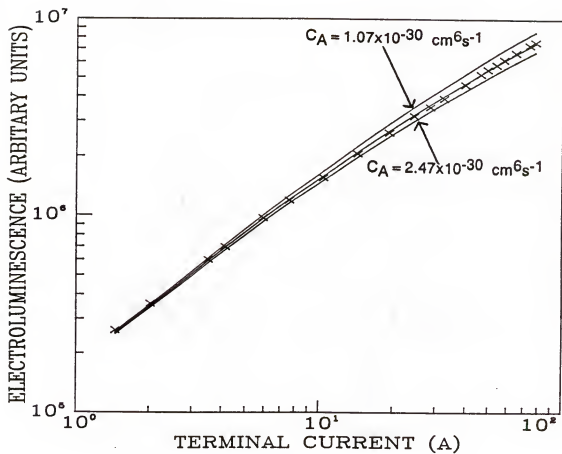


Fig. 5.7 Sensitivity of fitting to Auger coefficient.
The best fit is for $C_A = 1.77 \times 10^{-30} \text{ cm}^6 \text{ s}^{-1}$.

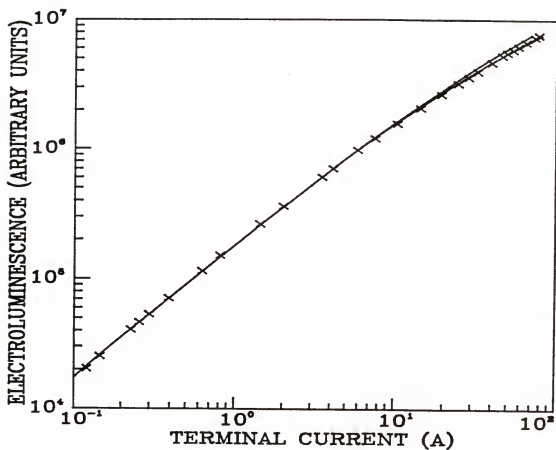
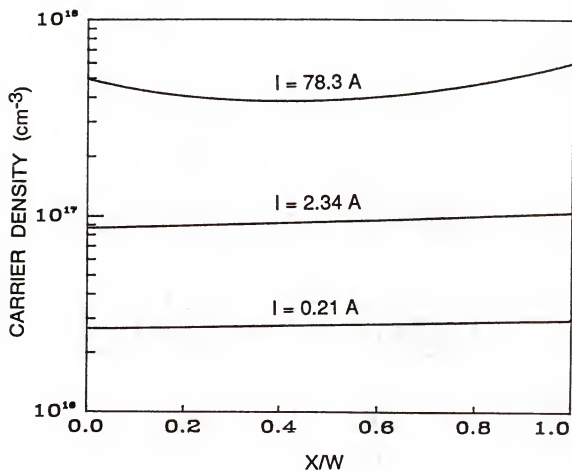


Fig. 5.8 Sensitivity of fitting to mobilities.

No doping variation of mobilities is assumed for the upper curve. The bottom curve assumes mobilities from ref. [56].

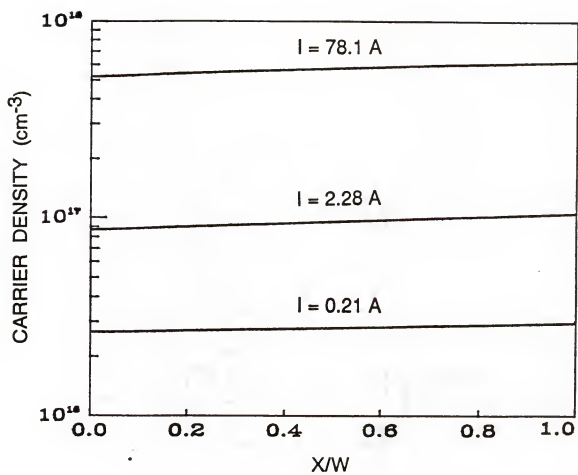


(a)

Fig. 5.9 Plasma densities across the p^- base with or without Auger recombination for different currents.

(a) $C_A = 1.77 \times 10^{-30} \text{ cm}^6 \text{ s}^{-1}$.

(b) $C_A = 0 \text{ cm}^6 \text{ s}^{-1}$.



(b)

Fig. 5.9 (continued)

recombination at high currents is almost flat through the p^- region. But it is not uniform for the case with the Auger recombination. The plasma densities for this case at $x = 0$ and $x = W$ are larger than in the middle region of the p^- layer, because the ambipolar diffusion length becomes shorter due to the Auger recombination.

We also checked the sensitivity of C_A to the mobilities and σ in this experiment. The C_A varies from $1.63 \times 10^{-30} \text{ cm}^6\text{s}^{-1}$ to $1.88 \times 10^{-30} \text{ cm}^6\text{s}^{-1}$ for $\sigma = 5.64 \times 10^{-18} \text{ cm}^2 \pm 20 \%$, it also changes 1.50×10^{-30} to $1.94 \times 10^{-30} \text{ cm}^6\text{s}^{-1}$ for $\mu_{n,p} = \mu_{n,p} \pm 20 \%$, where $\mu_{n,p}$ are well below their values at low injection.

The effects of J_{Op} and J_{On} on C_A are summarized in Table 5.2. The first column in Table 5.2 represents the data set for the best fit. The second column shows that even under the conditions of 20 % higher J_{Op} and 20 % less J_{On} than the values in the first column the C_A is same as in the best fit case. The third column is for the opposite case of the second. In this case we have the slightly different value for C_A .

5.3.2 Band Gap Narrowing and Transition Probabilities

The analysis presented in section Section 5.2 is based on two implicit assumptions. Zero band-gap narrowing and an electroluminescence intensity that is proportional to the pn product.

We checked qualitatively the assumption of zero band-gap narrowing for the plasma densities under study by measuring EL with and without interference filter between the $p^+/p^-/n^+$ diode and the

Table 5.2 Sensitivity of the saturation current to fitting.

I (A)		EL ₁	EL ₂	EL ₃
	J _{op} (A/cm ²)	4.4×10^{-13}	5.3×10^{-13}	3.5×10^{-13}
	J _{on} (A/cm ²)	4.3×10^{-13}	3.3×10^{-13}	5.7×10^{-13}
	C _A (cm ⁶ s ⁻¹)	1.77×10^{-30}	1.75×10^{-30}	1.96×10^{-30}
0.121		29779	29783	29316
0.394		99519	99645	99151
0.816		2.059×10^5	2.062×10^5	2.066×10^5
2.02		4.995×10^5	5.011×10^5	5.044×10^5
7.6		1.721×10^6	1.732×10^6	1.739×10^6
24.4		4.614×10^6	4.633×10^6	4.633×10^6
46.0		7.456×10^6	7.469×10^6	7.454×10^6
57.6		8.753×10^6	8.762×10^6	8.739×10^6
77.2		1.071×10^7	1.071×10^6	1.067×10^7

sensor. The interference filter has $1.1 \mu\text{m}$ transmission center wavelength and sharp cut-off characteristics for other wavelength. As shown in Table 5.3, the ratios of two ELs at various currents are almost same. This suggests that band-gap narrowing in the range of the plasma densities under study is either not existing or negligible.

The second assumption is equivalent to assuming that the probability for radiative transitions is independent of the injection level. This assumption has been experimentally verified by Gerlach and et al. for carrier plasma densities up to $2 \times 10^{17} \text{ cm}^{-3}$ [59]. To experimentally verify the same assumption for higher plasma densities, we excited a lightly doped silicon wafer with the second harmonic ($\lambda = 0.532 \mu\text{m}$) of a nanosecond pulsed NdYAG laser. The energy of the pulse was 5 mJ and it was attenuated by a factor of 1000 by a neutral density filter. The diameter of the beam was 3 mm. For a reflection coefficient (≈ 0.3) and an absorption coefficient of $0.9 \times 10^3 \text{ cm}^{-1}$, right after the pulse the plasma density at the surface becomes about $1.2 \times 10^{18} \text{ cm}^{-3}$ and decays exponentially inside the bulk according the absorption depth. The electroluminescence signal right after the pulse comes mostly from the excited surface and the first micron of depth where the plasma density changes from 1.2 to $0.45 \times 10^{18} \text{ cm}^{-3}$. The intensity of the laser was lowered by an additional factor of 2 by placing another neutral density filter between the first and the wafer. Thus the detected electroluminescence comes from a plasma density varying between 1.2 and $0.22 \times 10^{18} \text{ cm}^{-3}$. The transient electroluminescence

Table 5.3 Electroluminescence results measured with (EL₁) and without (EL₂) 1.1 μ m filter. EL₁ and EL₂ were measured at different sacles of lock-in amplifier.

CURRENT (A)	EL ₁ (mV)	EL ₂ (mV)
	(Without filter)	(With filter)
1.14	22.2	24.4
5.4	91.2	101.6
10.2	158.4	178.0
40.0	500.0	556.5
70.0	744.0	823.0

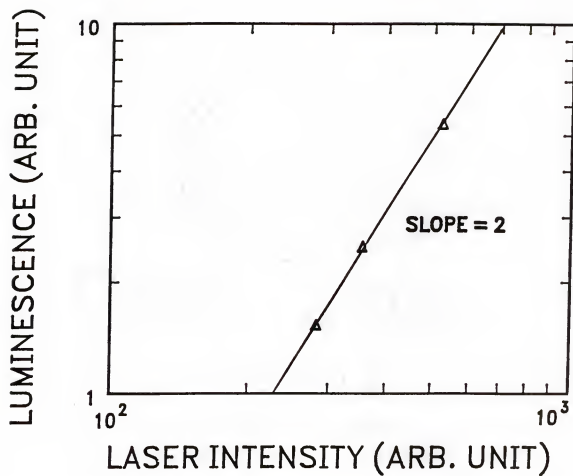


Fig. 5.10 Measured luminescence versus laser intensity.

signal was detected by a InGaAs detector placed from the other side of the wafer right across the excited spot. This is a convenient configuration because it completely filters the powerful laser pulse through the wafer. The signal was amplified by a current amplifier and displayed on a scope. Simultaneously, the laser pulse intensity was monitored by employing a beam splitter and a Si detector for a more accurate assessment of the relative intensity of the exciting signal. Figure 5.10 shows the peak of the electroluminescence intensity as a function of the laser intensity. The figure clearly demonstrates that the electroluminescence changes according to the square of the light intensity. Since the electroluminescence signal comes from plasma densities varying from 1.2 to $0.22 \times 10^{18} \text{ cm}^{-3}$, and the carrier density immediately following the pulse is proportional to the laser intensity, we conclude that EL is proportional to the pn product for carrier densities up to 10^{18} cm^{-3} .

5.4 Conclusions

The recombination lifetime under high injection conditions in the base of $n^+/p^-/p^+$ diode was investigated on the basis of the relation between electroluminescence and terminal current. For carrier plasma densities up to 10^{17} cm^{-3} the relation between the electroluminescence signal and the current through the device is linear and dominated by the heavily doped region recombination. This relation becomes sublinear for higher carrier density due to Auger recombination in the bulk of the p^- base. The Auger recombination

coefficient is extracted by fitting the experimental sublinearity with numerical solutions that express the electroluminescence signal as a function of the terminal current. In the 10^{17} to $6 \times 10^{17} \text{ cm}^{-3}$ carrier plasma density, the Auger coefficient was found to be $1.77 \times 10^{-30} \text{ cm}^6 \text{ s}^{-1}$.

CHAPTER SIX SUMMARY AND SUGGESTIONS

This dissertation deals with the device and physical parameters of bipolar transistors. The device parameters are dependent on the device model. The parameters investigated in this work are for the Gummel-Poon model.

The base resistance was obtained by measuring the input impedances of the common-base configuration at low current. The technique includes a correction for zeroing errors. The correction is based on comparing the directly measured common-base input capacitance with that obtained by combining the input capacitances of the two configurations for forward and inverse operation. The values for capacitances measured by the new method agree with the values from the standard method, which uses accurate dummy devices for zeroing. The advantage of the new method is that the accurate dummy devices are not necessary. Furthermore, the accuracy of the new method is about ± 0.3 fF, compared to 1-2 fF for the standard method. The standard method will not be good enough for future submicrometer-emitter transistors with junction capacitances of 1-5 fF. The junction capacitances, the base and collector saturation currents, and the device temperature are also extracted from the detail analysis of the base resistance dependence on bias. The method is also demonstrated on a heterojunction bipolar transistor.

A model to investigate the dependence of the emitter resistance on bias and the structural parameters was developed. The

model combines the emitter and contact crowding model with the distributed model for a transistor. The emitter resistance was evaluated by the circuit simulator SLICE using a power dissipation method. The general trends of the emitter resistance agree with the experimental results. The main conclusion of this topic is that when the emitter crowding becomes significant, the emitter resistance becomes current dependent. For the simplification of the analysis, the current gain β and the base sheet resistance were considered to be current independent. Their dependences can be included in the model for more accurate analysis.

A method for extraction of the collector resistance has been developed. The basic concept of the method is to use the substrate current of the integrated n-p-n transistor. This current is either the emitter or collector current of the parasitic p-n-p transistor, depending on biasing conditions. The parasitic transistor is turned on by the voltage drop on the collector resistance of the n-p-n transistor. The separation of the collector resistance components is possible by operating the p-n-p transistor in both upward and downward modes. It is difficult to accurately estimate the value for the collector resistance at high current because it is strongly effected by the high injection phenomena. Since the new method yields the current dependence of the collector resistance, it may be used as a tool for studying the high injection phenomena.

The recombination lifetime under high injection condition in the base of $n^+/p^-/p^+$ diode was investigated on the basis of the relation between the electroluminescence and terminal current. The Auger coefficient is extracted by fitting the experimental data with

numerical solutions that express the luminescence signal as a function of the terminal current. In the 10^{17} to $6 \times 10^{17} \text{ cm}^{-3}$ carrier plasma density, the Auger coefficient was found to be $1.77 \times 10^{-30} \text{ cm}^6 \text{ s}^{-1}$. The procedure used can be also applied to a heterojunction p/i/n structure.

APPENDIX A
INPUT IMPEDANCE FOR COMMON-EMITTER CONFIGURATION

To derive Z_{ine} we use the simplified equivalent circuit for the CE configuration shown in Fig. A.2. This circuit was derived from the hybrid- π circuit of Fig. A.1 by neglecting r_{μ} , r_c , and r_o . We further assume that $r_{\pi} \gg 1/\omega C_{\pi}$. The validity of all assumptions will be justified below. The result for Z_{ine} , neglecting the higher order frequency terms, is

$$\begin{aligned}
 Z_{ine} = & r_{bx} + r_{bi} \left\{ 1 - \frac{(1+g_m r_e) C_{sc} [(1+g_m r_e)(2C_{\mu} + C_{sc}) + 2C_{\pi}]}{[C_{\pi} + C_{\mu} + C_{sc} + g_m r_e (C_{sc} + C_{\mu})]^2} \right\} \\
 & + r_e \left(\frac{C_{\pi}}{(C_{\pi} + C_{\mu} + C_{sc}) + g_m r_e (C_{\mu} + C_{sc})} \right)^2 \\
 & - (j/\omega) \left(\frac{1+g_m r_e}{(C_{\pi} + C_{\mu} + C_{sc}) + (C_{\mu} + C_{sc}) g_m r_e} \right). \tag{A.1}
 \end{aligned}$$

Assuming further that $g_m r_e \ll 1$, we obtain

$$\begin{aligned}
 Z_{ine} = & r_{bx} + r_{bi} \left(\frac{C_{\pi} + C_{\mu}}{C_{\pi} + C_{\mu} + C_{sc}} \right)^2 + r_e \left(\frac{C_{\pi}}{C_{\pi} + C_{\mu} + C_{sc}} \right)^2 \\
 & + (1/j\omega) \frac{1}{C_{\pi} + C_{\mu} + C_{sc}}. \tag{A.2}
 \end{aligned}$$

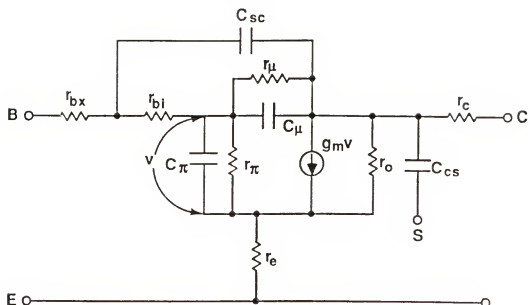


Fig. A.1 Small-signal equivalent circuit for the analysis.

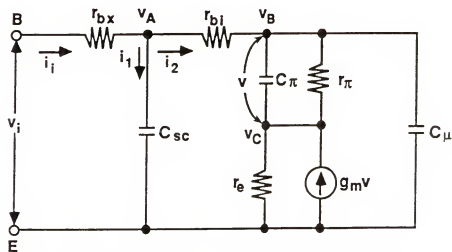


Fig. A.2 Simplified common-emitter equivalent circuit obtained from Fig. A.1 by neglecting the r_μ and r_o , and the collector series resistance r_c .

APPENDIX B
INPUT IMPEDANCE FOR COMMON-BASE CONFIGURATION Z_{inb}

Using the simplified diagram of Fig. B.1 and assuming $r_{\pi} \gg 1/\omega C_{\pi}$, $r_{bx} \ll 1/\omega C_{SC}$, and $r_{bi} \ll 1/\omega C_{\mu}$, we obtain

$$\begin{aligned}
 Z_{inb} &= \frac{(1+g_m r_e) + j\omega C_{\pi}(r_e + r_{bi} + r_{bx})}{j\omega C_{\pi} + g_m} \\
 &= r_e + r_{bi} \left(\frac{\omega^2 C_{\pi}^2}{g_m^2 + \omega^2 C_{\pi}^2} \right) + r_{bx} \frac{\omega^2 C_{\pi}^2}{g_m^2 + \omega^2 C_{\pi}^2} + \frac{g_m}{g_m^2 + \omega^2 C_{\pi}^2} \\
 &\quad - j \frac{1 - g_m(r_{bi} + r_{bx})}{\omega C_{\pi} + (g_m^2 / \omega C_{\pi})}.
 \end{aligned} \tag{B.1}$$

Assuming further that $g_m \ll \omega C_{\pi}$, and $g_m(r_{bi} + r_{bx}) \ll 1$, we have

$$Z_{inb} \approx r_e + r_{bi} + r_{bx} - j(1/\omega C_{\pi}). \tag{B.2}$$

The validity of the assumptions used to derive (A.2) and (B.2) was checked by calculating the input impedances Z_{ine} and Z_{inb} from the complete equivalent circuit shown in Fig. A.1 using SPICE. The inputs for the simulation were the measured parameters r_{π} (determined from the DC I_B - V_{BE} curve), r_{bx} , r_{bi} , r_e , C_{π} and C_{jc} . Reasonable estimated values were used for the other parameters, including parasitic capacitances. The agreement between the simple

results given by (A.2) and (B.2) and the circuit simulation was better than 1 percent for $V_{BE} < 0.45V$ in the frequency range from 10 to 100 MHz. This agreement shows the excellent accuracy of (2.1)-(2.4) used in this work.

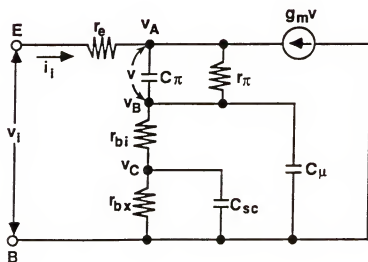


Fig. B.1 Simplified common-base equivalent circuit.

APPENDIX C FREE CARRIER ABSORPTION

The average number of photons emitted under an angle θ that is not absorbed by free carriers is proportional to

$$\exp(-\sigma \int_0^W n(y) \frac{dy}{\cos\theta} d\theta) \quad (C.1)$$

where σ is absorption cross-section, $n(y)$ is carrier density, and others are defined in Fig. C.1.

The total number of photons that are emitted under this angle and leaves the cell surviving the absorption is proportional to

$$\exp(-\sigma_n/\cos\theta) \cdot 2\pi \sin\theta d\theta \quad (C.2)$$

$$\text{where } \sigma_n = \sigma \int_0^W n(y) dy. \quad (C.3)$$

The $2\pi \sin\theta d\theta$ in (C.2) is a geometrical factor in the spherical coordinate for taking into account the light injected into all directions. The assumption used in the above derivation is the total attenuation is much smaller than 1.

Then, the total flux leaving the cell is proportional to

$$\int_0^{\pi/2} \exp(-\sigma_n/\cos\theta) 2\pi \sin\theta d\theta. \quad (C.4)$$

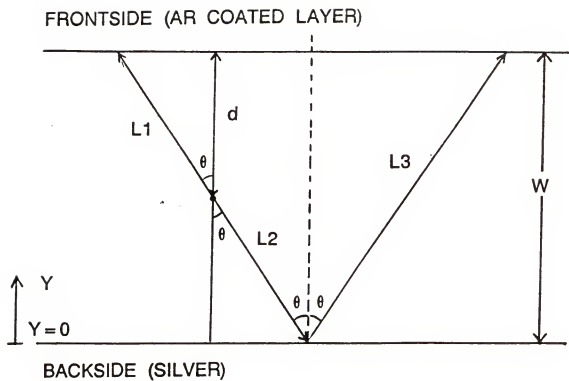


Fig. C.1 Schematic diagram for the analysis of free carrier absorption.

After changing variable, (C.4) becomes

$$\sigma_n \int_0^{1/\sigma_n} \exp(-1/x) dx. \quad (C.5)$$

For a certain number A which is larger than 1, (C.4) is expressed as

$$\begin{aligned} & \sigma_n \left(\int_0^A \exp(-1/x) dx + \int_A^{1/\sigma_n} \exp(-1/x) dx \right) \\ &= \sigma_n \left(\int_0^A \exp(-1/x) dx + \int_A^{1/\sigma_n} (1 - 1/x) dx \right) \\ &= 1 - \sigma_n \left(\ln (1/\sigma_n) + A - \ln A - \int_0^A \exp(-1/x) dx \right). \end{aligned} \quad (C.6)$$

The measured electroluminescence is

$$\left(1 - \sigma_n \left(\ln (1/\sigma_n) + A - \ln A - \int_0^A \exp(-1/x) dx \right) \right) EL, \quad (C.7)$$

where EL is calculated electroluminescence without the free carrier absorption.

REFERENCES

- [1] D. D. Tang and Paul M. Solomon, "Bipolar transistor design for optimized power-delay logic circuit," *IEEE J. Solid-State Circuits*, vol. SC-14, pp. 679-584, Aug. 1979.
- [2] T. Tashiro, H. Takemura, T. Kamiya, and F. Tokuyoshi, "An 80 ps ECL circuit with high current density transistor," in *IEDM Tech. Dig.*, pp 686-689, 1984.
- [3] R. W. Knepper, S. P. Gaur, F.-Y. Chang, and G. R. Srinivasan, "Advanced bipolar transistor modeling: process and device simulation tools for today's technology," *IBM J. Res. Develop.*, vol. 29, pp. 218-228, May 1985.
- [4] Neville H. Fletcher, "The high current limit for semiconductor junction devices," *IRE Proc.*, vol. 45, pp. 862-872.
- [5] A. Blicher, "Field-effect and bipolar power transistor physics," Academic Press., New York, 1981.
- [6] H. Murramann and D. Widmann, "Current crowding on metal contacts to planar devices," *IEEE Trans. Electron Devices*, vol. ED-16, pp. 1022-1024, Dec. 1969.
- [7] H. H. Berger, "Model for contacts to planar devices," *Solid-State Electron.*, vol. 15, pp. 145-158, 1972.
- [8] J. R. Hauser, "The effect of distributed base potential on emitter-current injection density and effective base resistance for stripe transistor geometries," *IEEE Trans. Electron Devices*, vol. ED-11, p 238, 1964.
- [9] J. J. Liou, F. A. Lindholm, and J. S. Park, "Forward-voltage capacitance and thickness of p-n junction," *IEEE Trans. Electron Devices*, vol. ED-34, pp. 1571-1579, July 1987.
- [10] K. Sukulal and K. N. Bhat, "Current gain of narrow-base transistors," *Solid-State Electron.*, vol. 29, pp. 311-316, Mar. 1986.
- [11] David L. Bowler and Fredrik A. Lindholm, "High current regimes in transistor collector regions," *IEEE Trans. Electron Devices*, vol. ED-20, pp. 257-263, Mar. 1973.

- [12] G. Rey, F. Dupuy, and J. P. Bailbe, "A unified approach to the base widening mechanisms in bipolar transistors," *Solid-State Electron.*, vol. 18, pp. 863-866, 1975.
- [13] George M. Kull, Laurence W. Nagel, Shiuh-Wuu Lee, Peter Lloyd, E. James Prendergast, and Heinz Dirks, "A unified circuit model for bipolar transistor including quasi-saturation effects," *IEEE Trans. Electron Devices*, vol. ED-32, pp. 1103-1113, Jun. 1985.
- [14] S. P. Gaur, P. A. Hahitz, Y.-J. Park, R. K. Cook, Y.-S. Huang, and L. F. Wagner, "Two-dimensional device simulation program: 2DP," *IBM J. Res. Develop.*, vol. 29, pp. 242-251, May 1985.
- [15] J. Luo and S. Graham, "A quasi 3-D base resistance R_B : Simulator for nonwalled emitter transistor," in *Proc. IEEE Bipolar Circuits Technol. Meeting (Minneapolis, Sept. 1987)*, pp. 13-17.
- [16] J. S. Park, A. Neugroschel, P. J. Zdebel, B.-Y. Hwang, and V. d. l. Torre, "Parameter extraction for advanced submicrometer-emitter bipolar transistor," in *Proc. SRC TECHCON 88 Conf.* (Dallas, TX, Oct. 12-14, 1988).
- [17] J. Logan, "Characterization and modeling for statistical design," *Bell Syst. Tech. J.*, vol. 50, pp. 1105-1147, Apr. 1971.
- [18] R. C. Jaegher and A. J. Brodersen, "Low-frequency noise sources in bipolar junction transistors," *IEEE Trans. Electron Devices*, vol. ED-17, pp. 128-134, Feb. 1970.
- [19] J. F. Gibbons, "Low-frequency noise figure and its application to the measurement of certain transistor parameters," *IRE Trans. Electron Devices*, vol. ED-9, pp. 308-315, May 1962.
- [20] J. Lindmayer, "Power gain of transistors at high frequencies," *Solid-State Electron.*, vol. 5, pp. 171-175, Jan. 1962.
- [21] W. E. Beadle, D. E. Dubarlos, and W. E. Eckton, "Design, fabrication and characterization of a germanium microwave transistor," *IEEE Trans. Electron Devices*, vol. ED-16, pp. 125-138, Jan. 1969.
- [22] J. S. Park, Arnost Neugroschel, and Fredrik A. Lindholm, "Numerical analysis and interpretation of small-signal minority-carrier transport in bipolar devices," *IEEE Trans. Electron Devices*, vol. ED-35, pp. 195-202, Feb. 1988.
- [23] Willy M. C. Sansen and G. Meyer, "Characterization and measurement of the base and emitter resistances of bipolar

- transistors," IEEE J. Solid-State Circuits, vol. SC-7, pp. 492-498, Dec. 1972.
- [24] Ian E. Getreu, "Modeling the bipolar transistor," Elsevier Scientific Publishing Company, New York, 1978.
 - [25] F. Hehert and D. J. Rouston, "Base resistance of bipolar transistors from layout details including two-dimensional effects at low currents and low frequencies," Solid-State Electron., vol. 31, pp. 283-290, Feb. 1988.
 - [26] A. Neugroschel, "Measurement of the low-current base and emitter resistances of bipolar transistors," IEEE Trans. Electron Devices, vol. ED-34, pp. 817-822, Apr. 1987; and Erratum, vol. ED-34, p. 2568, Dec. 1987.
 - [27] J. S. Park and Arnost Neugroschel, "Parameter extraction for bipolar transistors," IEEE Trans. Electron Devices, vol. ED-36, pp. 88-95, Jan. 1989.
 - [28] J. S. Park and A. Neugroschel, "Current dependence of the base and emitter series resistances of bipolar transistors," IEEE Bipolar Circuits Technol. Meeting (Minneapolis, Sept. 1987), pp. 78-81.
 - [29] J. E. Larry and R. L. Anderson, "Effective base resistance of bipolar transistors," IEEE Trans. Electron Devices, vol. ED-32, pp. 2503-2505, Nov. 1985.
 - [30] A. Neugroschel, J. S. Wang, F. A. Lindholm, "Evidence for excess carrier storage in electron-hole plasma in silicon transistors," IEEE Electron Device Lett., vol. EDL-6, pp. 253-255, Apr. 1984.
 - [31] E. A. Valsamakis, "Power dissipation calculation of the base spreading and contact resistance of transistors at low currents and low frequencies," IEEE Trans. Electron Devices, vol. ED-33, pp. 303-309, Feb. 1988.
 - [32] R. B. Chawla and H. K. Gummel, "Transition region capacitance of diffused p-n junctions," IEEE Trans. Electron Devices, vol. ED-18, pp. 178-195, Mar. 1971.
 - [33] J. J. Liou and F. A. Lindholm, "High-forward-voltage junction capacitance including effects of excess carrier storage in electron-hole plasma," J. Appl. Phys., vol. 62, pp. 3853-3856, Nov. 1986.
 - [34] J. A. Hutchby, "High-performance p-n-p AlGaAs/GaAs heterojunction bipolar transistors: A theoretical analysis," IEEE Electron Device Lett., vol. EDL-7, pp. 108-111, 1986.

- [35] S. Tan and A. G. Milnes, "Consideration of the frequency performance potential of GaAs homojunction and heterojunction transistors," *IEEE Trans. Electron Devices*, vol. ED-30, pp. 1289-1294, Oct. 1983.
- [36] J. Choma, Jr., "Error minimization in the measurement of bipolar collector and emitter resistances," *IEEE J. Solid-State Circuits*, vol. SC-11, pp. 318-322, Apr. 1976.
- [37] A. Z. Incecik, "Computer-aided determination of emitter and collector resistance of integrated bipolar transistors," *IEEE J. Solid-State Circuits*, vol. SC-14, pp. 1108-1111, Dec. 1979.
- [38] Stephen J. Proctor, Loren W. Lindholm, and Jeffrey A. Mazer, "Direct measurements of interfacial contact resistance, and interfacial contact layer uniformity," *IEEE Trans. Electron Devices*, vol. ED-30, pp. 1535-1542, Nov. 1983.
- [39] J. G. J. Chern and W. G. Oldham, "Determining specific contact resistivity from contact end resistance measurements," *IEEE Electron Device Lett.*, vol. EDL-5, pp. 178-180, May 1984.
- [40] M. Finetti, A. Scorzoni, and G. Soncini, "Lateral current crowding effects on contact resistance measurements in four terminal resistor test patterns," *IEEE Electron Device Lett.*, vol. EDL-5, pp. 524-526, Dec. 1984.
- [41] W. M. Loh, K. Saraswat, and R. W. Dutton, "Analysis and scaling of Kelvin Resistors for extraction of specific contact resistivity," *IEEE Electron Device Lett.*, vol. EDL-6, pp. 105-108, Mar. 1985.
- [42] W. M. Loh, S. E. Swirhun, E. Crabbe, K. Sarawat, and R. M. Swanson, "An accurate method to extract specific contact resistivity using Cross-Bridge Kelvin Resistors," *IEEE Electron Device Lett.*, vol. EDL-6, pp. 441-443, Sept. 1985.
- [43] S. E. Swirhun, W. M. Loh, R. M. Swanson, and K. C. Sarawat, "Current crowding effects and determination of specific contact resistivity from contact end resistance (CER) measurements," *IEEE Electron Device Lett.*, vol. EDL-6, pp. 639-641, Dec. 1985.
- [44] Geoffrey Reeves and H. Barry Harrison, "Determination of contact parameters of interconnecting layers in VLSI circuit," *IEEE Trans. Electron Devices*, vol. ED-33, pp. 328-334, Mar. 1986.
- [45] Kwok K. NG and William T. Lynch, "The impact of intrinsic series resistance on MOSFET scaling," *IEEE Trans. Electron Devices*, vol. ED-34, pp. 503-511, Mar. 1987.

- [46] A. Y. C. Yu, "Electron tunneling and contact resistance of metal-silicon contact barrier," *Solid-State Electron.*, vol. 13, pp. 239-247, 1970.
- [47] Tak H. Ning and Denny D. Tang, "Method for determining the emitter and base series resistances of bipolar transistors," *IEEE Trans. Electron Devices*, vol. ED-31, pp. 409-412, Apr. 1984.
- [48] William D. Mack and Mark Horowitz, "Measurement of series collector resistance in bipolar transistors," *IEEE J. Solid-State Circuits*, vol. SC-17, pp. 767-773, Aug. 1982.
- [49] J. Dziwior and W. Schmid, "Auger coefficients for highly doped and highly excited silicon," *Appl. Phys. Lett.*, vol. 31, pp. 346-348, Sept. 1977.
- [50] K. G. Svantesson and N. G. Nilsson, "Measurement of Auger recombination in silicon by laser excitation," *Solid-State Electron.*, vol. 21, pp. 1603-1608, 1978.
- [51] I. V. Grekhov and L. A. Delimova, "Auger recombination in silicon," *Sov. Phys. Semicond.*, vol. 14, pp. 529-532, May 1980.
- [52] Yu. Vaikus and V. Grivitskas, "Dependence of the rate of interband Auger recombination on the carrier density in silicon," *Sov. Phys. Semicond.*, vol. 15, pp. 1102-1108, Oct. 1982.
- [53] E. Yablonovitch and T. Gmitter, "Auger recombination in silicon at low carrier densities," *Appl. Phys. Lett.*, vol. 49, pp. 587-589, Sept. 1986.
- [54] Ronald A. Sinton and Rich M. Swanson, "Recombination in high injected silicon," *IEEE Trans. Electron Devices*, vol. ED-34, pp. 1380-1387, June 1987.
- [55] K. Misiakos and Arnost Neugroschel, "Lifetime and diffusivity determination from frequency-domain transient analysis," *IEEE Electron Device Lett.*, vol. EDL-8, pp. 358-360, Aug. 1987.
- [56] B. Jayant Baliga, "Modern power devices," John Wiley & Sons, New York, Chapter 2, p 12, 1987.
- [57] K. G. Svantesson, "Determination of the interband and the free carrier absorption constants in silicon at high-level photoinjection," *J. Phys. D: Appl. Phys.*, vol. 12, pp. 425-436, 1979.
- [58] C. M. Horwitz and R. M. Swanson, "The optical (free-carrier) absorption of a hole-electron plasma in silicon," *Solid-State Electron.*, vol. 23, pp. 1191-1194, 1980.

- [59] W. Gerlach, H. Schlangennotto, and H. Maeder, "On the radiative recombination rate in silicon," *Phys. Stat. Sol.*, vol. (a) 13, pp. 277-283, 1972.

BIOGRAPHICAL SKETCH

Ju-Sung Park was born in Jinju, Korea, on December 19, 1953. He received the B.S. degree in electronics engineering from Pusan National University, Pusan, Korea, in 1976 and the M.S. degree in electrical engineering from the Korea Advanced Institute of Science, Seoul, Korea, in 1978. Since 1985 he has been working toward the Ph.D. at the University of Florida, Gainesville, Florida, with emphasis on the parameter extraction of bipolar transistors.

From March 1978 to July 1985, he was with the Electronics and Telecommunication Research Institute (ETRI), Taejun, Korea, where he worked as a Senior Research Engineer and as the Manager of IC design group. While at ETRI he designed several bipolar analog ICs and was in charge of developing VCR ICs and CMOS 8-bit microcomputer


His research interests are IC design, device physics and modeling.

I certify that I have read this study and that in my opinion it conforms to acceptable standards of scholarly presentation and is fully adequate, in scope and quality, as a dissertation for the degree of Doctor of Philosophy.



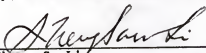
Arnost Neugroschel, Chairman
Professor of Electrical Engineering

I certify that I have read this study and that in my opinion it conforms to acceptable standards of scholarly presentation and is fully adequate, in scope and quality, as a dissertation for the degree of Doctor of Philosophy.




Fredrik A. Lindholm
Professor of Electrical Engineering

I certify that I have read this study and that in my opinion it conforms to acceptable standards of scholarly presentation and is fully adequate, in scope and quality, as a dissertation for the degree of Doctor of Philosophy.



Sheng S. Li
Professor of Electrical Engineering

I certify that I have read this study and that in my opinion it conforms to acceptable standards of scholarly presentation and is fully adequate, in scope and quality, as a dissertation for the degree of Doctor of Philosophy.



Gys-Bosman
Associate Professor of Electrical Engineering

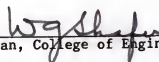
I certify that I have read this study and that in my opinion it conforms to acceptable standards of scholarly presentation and is fully adequate, in scope and quality, as a dissertation for the degree of Doctor of Philosophy.



Timothy James Anderson
Professor of Chemical Engineering

This dissertation was submitted to the Graduate Faculty of the College of Engineering and to the Graduate School and was accepted as partial fulfillment of the requirement for the degree of Doctor of Philosophy.

August 1989



Dean, College of Engineering

Dean, Graduate School